The Role of Sulfur Species in Establishing the Corrosion Reactions in Refinery Metallurgies

by

Justin Natale Lepore

A thesis submitted in partial fulfillment of the requirements for the degree of

Master of Science

in

Materials Engineering

Department of Chemical and Materials Engineering
University of Alberta

Abstract

This thesis is focused on the studying the role that model sulfur-containing molecules have in corrosion reactions on relevant metallurgies. This was done by using a design of experiments where a number of sulfur-based compounds were reacted with various metallurgies. The 8 model sulfur compounds were chosen to represent a broad set of structures: two mercaptans (M1 and M2) with M2 having a longer chain than M1, an aliphatic sulfide and disulfide (LS and LS), an aromatic sulfide and disulfide (RS and RD), and two cyclic thioethers (C1 and C2) with C2 containing more hydrogen than C1. The 5 metallurgies used were: 5 chrome alloy, 9 chrome alloy, 410 steel, 316 stainless steel, and carbon steel.

In the first round of experiments, the compounds were tested by placing 5000 ppm by weight of sulfur of a respective sulfur compound into 9 mL of Paraflex white mineral oil along with a rectangular carbon steel coupon in a sealed reactor, pressurized to 40 psig, and held at a medium temperature for a fixed set of time. The next round of experiments replaced the rectangular coupons with 1-inch extruded wire sections 200 μm in diameter of the five metals. Each of the eight compounds were reacted with the carbon steel wires at two process temperatures, a medium temperature and a medium-high temperature, and two experiment times, a short experiment time and a long experiment time. The remaining four metallurgies (5Cr, 9Cr, 410 steel, and 316 stainless steel) were reacted with each of the eight sulfur compounds only at the most extreme conditions of the medium-high temperature and reacted for the long experiment time. Once again, for these experiments the compounds were measured to 5000 ppm by weight of sulfur and placed with 9 mL of Paraflex white mineral oil into the sealed and pressurized reactor along with the extruded metal wire. After reacting, these wires were mounted in nickel-infused epoxy and polished for SEM and EDXS analysis, or left unmounted and used for XRD analysis. Overall, in these corrosion

experiments, the 316 stainless steel remained nearly pristine after reacting with any of the sulfur compounds, while the carbon steel samples were heavily corroded.

To react the metals with pure H_2S, a sealed tube furnace was sparged and filled with 5000 ppm H_2S gas (5174 ppm H_2S, 10.19% hydrogen, argon balance) and heated to either a medium or medium-high temperature with the extruded metal wires supported vertically inside in the tube. After reacting for either a quick, short, or long experiment time, these wires were then removed and mounted in nickel-infused epoxy and polished for SEM and EDXS analysis.

The decomposition temperature of each sulfur compound was recorded as the lowest measured temperature that H_2S was detected in the headspace gas of the sealed reactor after reacting for a long experiment time at the respective temperature in pure Paraflex mineral oil. This was determined by either increasing or decreasing the reaction temperature in 5 °C increments until the temperature was found such that H_2S was first detected. As expected given their thermal stability, the cyclic thioethers, C1 and C2, did not decompose into H_2S in any of our experiments, up to the limit of temperatures we were capable of reaching with our equipment. On the other hand, the aliphatic disulfide, LD, readily decomposed into H_2S at temperatures lower than the medium corrosion experiment temperature, likely due to the overall structure and properties of the compound.

Preface

Chapter 1 of this thesis gives an outline of corrosion in general, as well as an introduction to fouling, coking, and heavy oil analysis.

Chapter 2 explains the experimental procedure for working with and analyzing the samples used in this thesis.

Chapter 3 goes on to explain the results from the experiments, and is sub-sectioned to organize the results from the different experimental setups.

Chapter 4 explains and provides some background information to further discuss some special cases that revealed themselves in the experimental results.

Chapter 5 provides a conclusion to summarize the concepts written.

Dedication

This thesis is dedicated to my parents, Mario and Adriana, and my sister Sophia, for their complete support during my time as a student. Thank you.

Acknowledgements

First, I would like to thank my supervisor Dr. David Mitlin for his support and guidance throughout my graduate program and summer research. As well, I would like to thank Dr. Thomas Thundat for being my co-supervisor. The numerous professors I had over the years at the University of Alberta also deserve a thank-you for everything they have taught me.

I would also like to thank Paul Concepcion, Kai Cui, and the rest of the technical staff at the National Institute for Nanotechnology for their time spent maintaining the instruments needed for this research. As well, thank you to the support staff and the security staff for keeping the entire facility running safely and smoothly.

I would like to thank BP for their interest and funding in this project. My graduate studies would not have been possible without their support.

Lastly, I would like to thank Tyler Stephenson, Michael Hazelton, and the many previous students that have been through the Mitlin Group for always being friendly and helpful. I have learned a lot from all of you.

Table Of Contents

List of Figures

List of Tables

List of Equations

$$R_f = \Phi_d - \Phi_r$$

$$\rho = 1033\text{-}13.69H + 13.85S + 115.7N$$

$$°API = \frac{141.5}{s.g. @ 15.6\,℃}\text{-}131.5 = \frac{1.415 \times 10^5}{\rho}\text{-}131.5$$

Chapter 1
Introduction to Corrosion

1-1: Corrosion and Its Impact

Corrosion and similar phenomena have a persistent financial and industrial impact in the oil and gas industry. The total sum of corrosion from all industries can reach nearly $300 billion a year in the USA alone.[1] In many industrialized nations, the cost of corrosion per year roughly correlates to approximately 3-5% of the GDP of that nation.[1,2]

This financial cost is both direct and indirect. Direct costs of corrosion include capital costs, such as the cost of replacement parts, control costs for the maintenance and repair of parts, and design costs for protective measures such as corrosion inhibitors and protective coatings.[2] Indirect costs of corrosion include the cost of plant shutdown while corroded parts are dealt with, the loss of products through leaking in corroded liquid transport systems, and the contamination of a product with corroded particulates from a bulk material.[2]

Table 1.1: Approximate annual cost of corrosion in the oil and gas industry.[3,4]

Cause	Annual Cost (Millions of dollars)
Surface pipelines and facilities	$589
Downhole tubing	$463
Capital expenditures related to corrosion	$320
Total	$1,372

Financial estimates for the annual cost of corrosion in the oil and gas industry can reach over a billion dollars, and are approximately summarized in Table 1.1.[3,4]

1-2: Corrosion, Fouling, and Coking in the Oil and Gas Industry

In the oil and gas industry, corrosion often takes the form of fouling. Fouling is a well-studied process[5-12] that can be simply explained as “the accumulation and formation of unwanted

materials on the surfaces of processing equipment".[5] This accumulation of deposits and materials, usually referred to as the foulant layer, poses significant problems. In heat-transfer applications, the foulant layer acts as insulation against the direction of heat-flow, leading to decreased efficiency in the overall system and wasted energy. In pipeline systems, a foulant layer can decrease the internal diameter of the pipe by a finite amount, leading to pressure changes in the system and requiring pumps to expend more energy. Refineries and heavy-oil upgraders in particular often suffer from fouling, due to the various heat-transfer systems used in refining or upgrading crude oils. In general, a foulant layer can directly attack the metal surface it rests on, often resulting in mechanical failure for the metal.

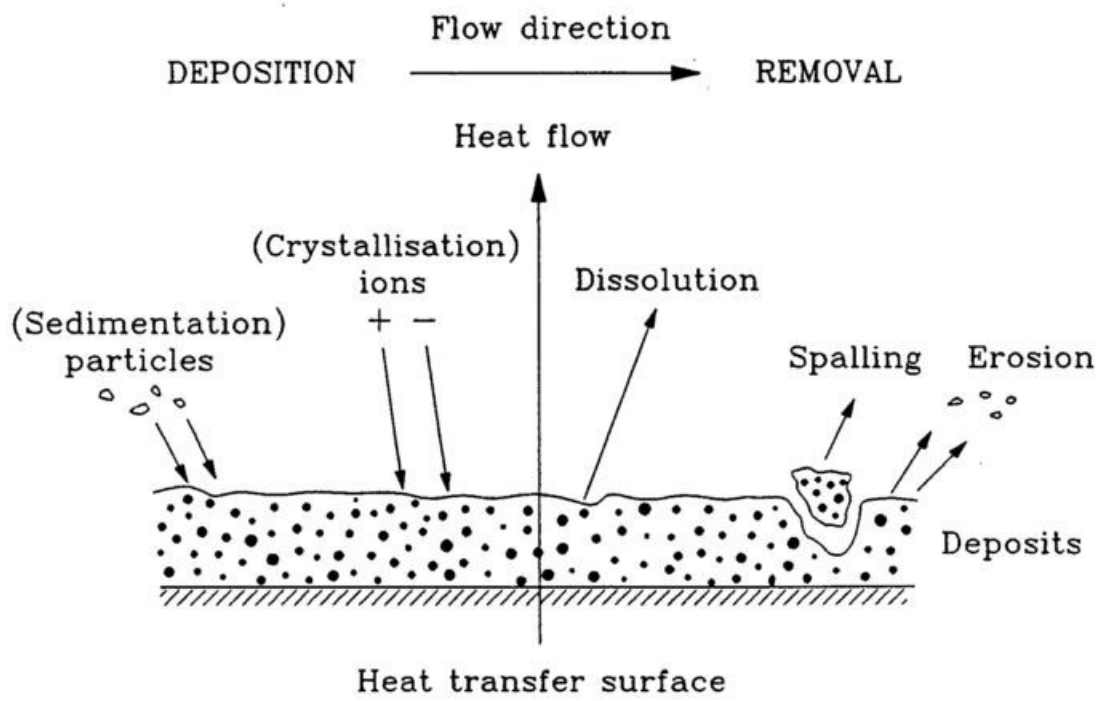

Figure 1.1: Schematic of fouling on a heat transfer surface. Image sourced from Heat Exchangers - Basics Design Applications, pg. 508, ISBN: 978-953-51-0278-6.[12]

Oftentimes, the foulant layer in an aqueous system is the result of mineral scale such as inorganic salts[13], or of biological organic material, also known as biofoulant.[14,15] In petroleum systems, on the other hand, the foulant layer is usually comprised of carbonaceous deposits called

petroleum coke, or simply coke. In the context of refining, coke is defined as a carbon-rich material that is insoluble in toluene or other aromatic solvents.[16] Understanding the nature of coking reactions from heavy oil and its constituents is a crucial first step in attempting to recognize and mitigate fouling.

A fouling factor can be calculated in order to quantify the fouling rate of a system. In the most general terms, the fouling factor R_f is simply the rate of foulant removal, Φ_r, subtracted from the rate of foulant deposition, Φ_d, written as Equation 1.1.[7] These rates can be expressed in terms of the mass change of foulant per area per second ($kg \cdot m^{-2} \cdot s^{-1}$), the thermal resistance of a fouled area ($m^2 \cdot K \cdot W^{-1}$), or simply as a velocity describing the increase in the foulant layer thickness per second ($m \cdot s^{-1}$).[7]

Equation 1.1 $$R_f = \Phi_d - \Phi_r$$

Petroleum is not a single-component system, rather it is a complex mixture of many organic components such as carbon, hydrogen, sulfur, nitrogen, and inorganic compounds such as minerals and salts, as well as a number of biological species. All of these components have different molecular weights and molecular structures. Although the hydrocarbon component of crude oil can comprise nearly 97% of the mixture, the remaining 3% non-hydrocarbon content, namely the hydrogen, sulfur, nitrogen, and oxygen, play a large part in determining the processability of the crude oil feedstock.[17] Hydrogen, sulfur, and nitrogen have such an effect on the properties of a crude oil that the density of a crude can be approximately calculated using the empirical equation written as Equation 1.2.[18] Here density ρ is solved in kg/m^3, and H, S, and N respectively refer to the hydrogen, sulfur, and nitrogen content in wt%.

Equation 1.2 $$\rho = 1033 - 13.69H + 13.85S + 115.7N$$

Due to the complexity of accounting for all of these different species in crude oil, various analysis methods have been used to organize the components into groupings based on physical

properties. The PIANO definition is one such method, splitting crude oil into fractions of paraffins, iso-paraffins, aromatics, napthenes, and olefins. A second grouping is the SaRA system, which organizes the species into saturates, aromatics, resins, and asphaltenes. The SaRA system allows components to be separated through solubility properties. Namely, the asphaltenes are toluene soluble but heptane insoluble, while the other three components are heptane soluble.

Figure 1.2, sourced from the work of Wiehe[19] shows coke formation (called "toluene insolubles") formed during the heating of three different crude oils, each with different amounts of asphaltene content. At 400 °C, coke formation begins nearly instantly with the 100% asphaltene stock. With the 25% and 0% asphaltene samples, however, an induction period is observed before coke formation, with the 0% asphaltenes sample taking longer to form coke than the 25% sample.

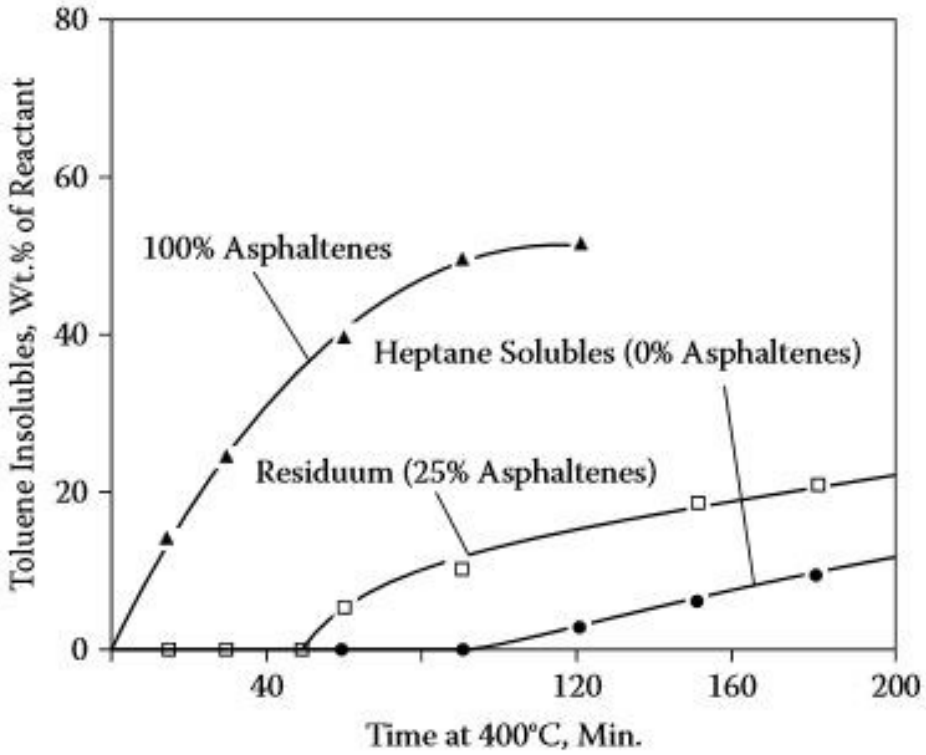

Figure 1.2: Kinetics of coke formation for three crude oils. Image sourced from Process Chemistry of Petroleum Macromolecules, pg. 104, ISBN: 978-1-57444-787-3.[19]

Figure 1.3, also from Wiehe,[19] shows the formation of crude oil components as the oil sample is held at a temperature of 400 °C. Recall again that "toluene insolubles" refers to coke, and note that coke formation begins at the point of maximum asphaltene content.

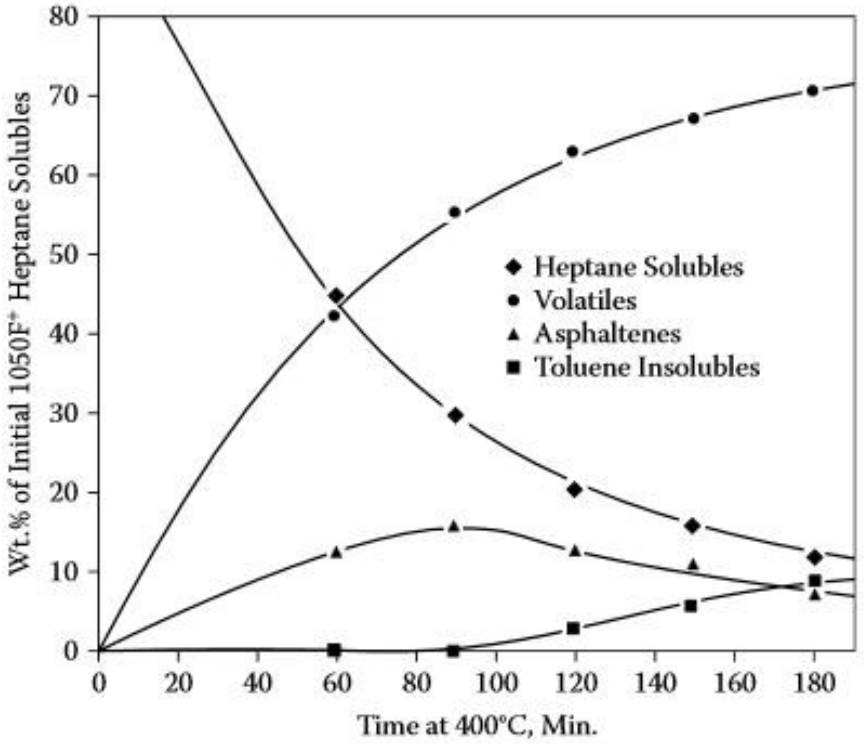

Figure 1.3: Kinetics of product formation from crude oil at 400 °C. Image sourced from Process Chemistry of Petroleum Macromolecules, pg. 104, ISBN: 978-1-57444-787-3.[19]

1-3: The Role of Sulfur in Corrosion and Fouling

Crude oil can be classified as being either sweet or sour. Sweet crude oil is usually defined as that which has a sulfur content less than 0.5 wt%, while sour crude oil has a sulfur content greater than 0.5 wt%.[18] This classification has become important in the 20th century as heavy oil production has increased. The supply of sweet crudes are diminishing, leading to the increasing exploitation and refining of sour opportunity crudes. These heavy, sour, highly acidic crudes are often highly acidic and high in sulfur content, along with nitrogen, aromatics, and other undesirables.[20]

Sulfur is known to be a corrosive substance. Sulfur in crude oil at a mass concentration greater than 0.2% w/w is known to be corrosive to carbon steel and low-alloy steels,[20] and even residual sulfur in gasoline will corrode automobile engine parts.[17] Including the corrosive nature of sulfur, Speight[17] lists five common reasons for removing sulfur from a crude oil feedstock: 1) the reduction of corrosion during handling and refining, 2) ensuring that the processed products have an acceptable odour, 3) increasing the performance of gasoline, 4) decreasing smoke formation from kerosene, and 5) improving the burning characteristics and environmental properties of other fuels. Removing sulfur from crude oil is usually done with one of three techniques[17]:1) thermal cracking, 2) catalytic cracking or other chemical methods, and 3) hydrodesulfurization.

Heavy crude is defined by Gray[18] as crude that has an API gravity between 10 and 19, a density of 900 to 1000 kg/m³, and a viscosity between 10^2 and 10^5 mPa·s. Figure 1.4, also from Gray,[18] neatly plots the classification of petroleum types based on their viscosity and density. The heavy oil, extra heavy oil, and bitumen regions are of the most interest since these types of petroleum tend to have the highest levels of sulfur content. Equation 1.3 shows the equation used to calculate API gravity, using the standard gravity at 15.6 °C, or the density in kg/m³. Referring back to Equation 1.2 and relating it to Equation 1.3, it is seen that the density of a crude increases, and the API gravity decreases, as the sulfur content increases.

Equation 1.3 $$°API = \frac{141.5}{s.g.@\ 15.6\ ℃} - 131.5 = \frac{1.415\ \times 10^5}{\rho} - 131.5$$

Table 1.2, sourced by the work of Gray et al.,[18,21] shows the properties of a light crude and two heavy crudes. As expected, the API gravity of the heavy crudes is less than the light crude, and the sulfur content of the heavy crudes is substantially greater than that of the light crude.

Table 1.2: Properties of a light crude compared to two heavy crudes. Table sourced from Upgrading Oilsands Bitumen and Heavy Oil, pg. 16, ISBN: 978-1-77212-035-6.[18,21]

Property	Light Crude	Cold Lake Bitumen	Athabasca Bitumen
API Gravity	40.8	10	9
Sulfur, wt%	0.3	4.4	4.9
Nitrogen, wt%	0.08	0.4	0.5
Metals, wppm	3.2	220	280
Viscosity, $m^2/s \times 10^6$ at 40 °	4	5000	7000
Vacuum Residue, 524 °C+,Liquid Vol%	12.9	52	52

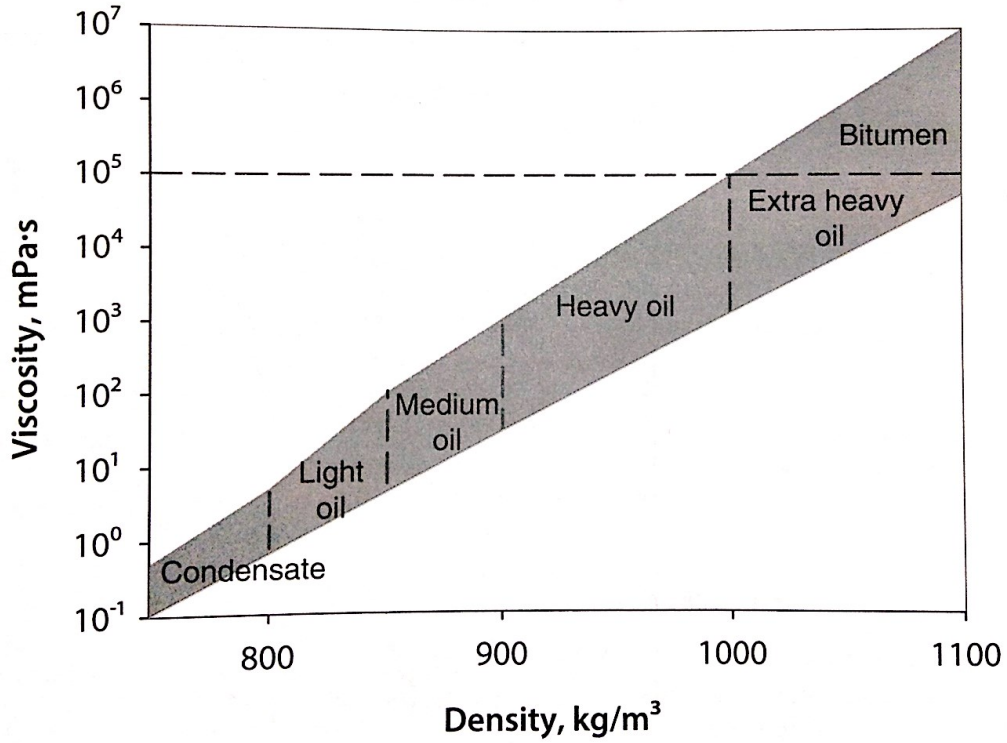

Figure 1.4: Classification of crude oils and bitumen as a function of their viscosity and density. Image sourced from Upgrading Oilsands Bitumen and Heavy Oil, pg. 2, ISBN: 978-1-77212-035-6.[18]

When processing high S and high TAN (naphthenic acids) crudes, corrosion is one of the major challenges in the refineries because it impacts the safety, reliability, and performance of the refining operation. A corrosion model that looks at sulfur compounds such as H_2S, mercaptans, sulfides, and disulfides would provide useful insights that can be applied to industry. It is widely accepted that these sulfur compounds will convert to H_2S under thermal conditions and that H_2S will react with steel to cause corrosion. This claim implies that all sulfur compounds will need to convert to H_2S to be corrosive. However there is no data in the available scientific literature either

supporting or discrediting this assertion. In order to improve the accuracy of the existing corrosion models, it is critical to understand the chemistry of sulfidic corrosion. Understanding the chemistry of how various sulfur compounds behave under thermal conditions in converting to H_2S will help to identify the relevant kinetic parameters, the real corrodents, and how to structure the kinetic equations so that we can construct a better corrosion model for accurate prediction.

Non-aqueous corrosion in an oil-refining environment involves a complex interplay between flow rate, turbulence, and temperature. The temperature-dependent attack of naphthenic acids and sulfur species is opposed by natural and externally introduced corrosion barriers on the metal surface in the form of (partially) adherent sulfides and oxides.[22,23,24,25] Depending on the flow rate and the metal geometry, flow may be turbulent or laminar. Volatiles that evolve due to cracking and polymerization reactions in the oil may also create a fluctuating metal-gas interface. In addition, with the corrosion of Fe by H_2S ($Fe + H_2S \rightarrow FeS + H_2$), the generated hydrogen bubbles may adhere to the metal surface. The hypothetical corrosion-protection scenarios may be subdivided into systems that do not form protective oxides (non-passivating) and systems that do form them (passivating). Though the exact metallurgy that separates passivating from non-passivating alloys is dependent on the corrosion conditions (e.g. temperature and activity of corroding species in the liquid and/or gas phase), one can generally state that the non-passivating systems are low/zero-Cr alloys while the passivating systems are high-Cr alloys. The behaviour of steel metallurgies with intermediate Cr content tends to be perhaps the most environment-dependent.

Analogous surface formations have been described in the literature for various H_2S-containing process conditions, albeit with no real agreement regarding the exact structure, composition, morphology, and degree of imparted protection from each layer.[26,27,28,29,30,31]

Moreover there is significant disagreement in literature regarding even some of the essential basics, such as the actual structure, protectiveness, or even the existence of the inner sulfide or inner sulfide-oxide layers reported to be present in Cr-containing alloys.[32,33,34] It is generally believed that for low-Cr and carbon-steels there is a sulfide-based bilayer that is formed on the metal surface, with the outer layer being caused by the outward diffusion of mostly Fe and the inner layer being caused by the inward diffusion of the reactive gas species. In the case of high-Cr alloys, a stable Cr_2O_3 layer is formed which acts as a relatively effective barrier for both the outward diffusion of Fe (via Fe^{2+} cation through the bulk oxide) and the inward diffusion of corrosive molecules. For example, work by Mitlin et al.[35] demonstrated that it is this Cr-based barrier that is responsible for the significantly reduced corrosion-fouling rates of stainless steel versus the corrosion-fouling rates of pure Fe wires exposed to elevated-temperature vacuum resid.

Various rate laws have been reported for corrosion of steels as a function of time, alloy metallurgy, and reaction temperature. One critical and often reported phenomenon is "runaway corrosion," which causes a transition from a decaying ~ $(\text{time})^{1/2}$ dependence of corrosion rate to either a linear or even an exponential time dependence.[34] This highly dangerous transition has been attributed to the localized growth of an inner sulfide layers, followed by localized cracking. Under flow conditions, this may result in the subsequent delamination of the entire protective multilayer oxide/sulfide, leaving exposed the bare metal. Catastrophically high corrosion rates would result if this phenomenon was cyclical, leaving the metal surface essentially unprotected.

While one can generally state that the corrosion species in the oil are naphthenic acids (R-COOH), mercaptans (R-SH), sulfides, and polysulfides, the real corrosion mechanisms are significantly more complicated and are also poorly understood. Thiophenes, which are also present in the oil, are generally considered benign, but their interaction with the more corrosive molecules

and any resultant corrosive or protective synergy remains ambiguous. The concept that the total sulfur content in the oil may directly relate to the corrosion rate for a given metallurgy and temperature was recently shown to be inaccurate for both carbon-steels and Cr steels.[34] The same is true when correlating the corrosivity of the oil to its total acid number (TAN). For example, several authors[36,37,38,39] reported that neither the total sulfur content nor the TAN of a given oil is an adequate predictor of its net corrosivity. A much more involved interaction between the structure of the sulfur-containing or naphthenic acid molecule, their boiling points, and the process temperature has to be taken into account. Another study conducted on Cu alloys not only demonstrated the mercaptan molecular-structure dependence of corrosion rates, it also highlighted a significant synergy of various mercaptans with elemental sulfur for accelerating corrosion reactions.[40]

As refineries begin to process heavier crude oils, it is apparent that it is necessary to understand the role of sulfur in refining processes and the corrosive properties of sulfur on refinery equipment.

Chapter 2
Experimental Details

2-1: Experimental Details

The target metallurgies were A) carbon-steel, B) 5 Chrome alloy, C) 9 Chrome alloy (P91), D) SS 316, and E) SS 410. The metal coupons were exposed to a reaction media containing model sulfur compounds. The sulfur model compound was dissolved in white oil at a concentration corresponding to sulfur levels found in crude oil. The sulfidic corrosion experiments were performed in 15 mL sealed static autoclave reactors, fabricated from 316 stainless steel Swagelok tubing with an outer diameter of 0.75 inches. Figure 2.1 depicts a rendering of a sealed reactor. The model sulfur-containing compounds used are presented in Table 2.1.

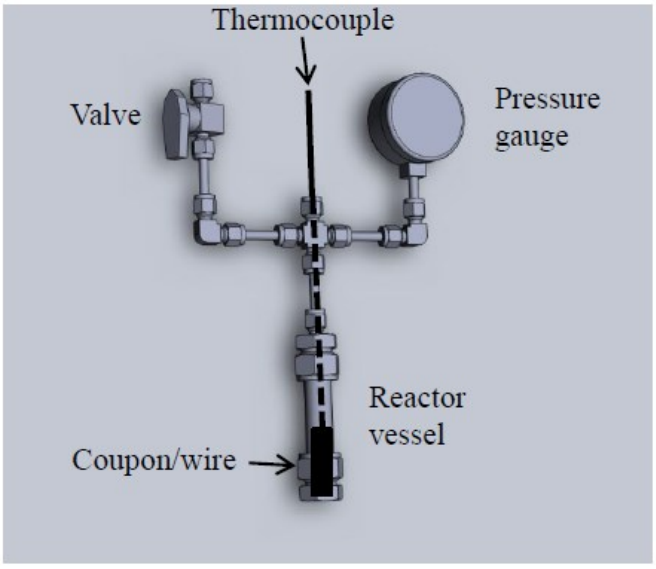

Figure 2.1: Schematic of the sealed static autoclave reactor used for the corrosion experiments. Credit for drawing this figure is given to Michael Hazelton.

For each experiment, a cleaned wire of the chosen metallurgy was placed in a clean reactor, and 9 mL of Paraflex HT-1000 white mineral oil were measured and poured in the reactor. 5000 ppm of the respective sulfur compound was then mixed-in, and the top unit of the reactor was then screwed on and tightened. The reactor was sparged by pressuring the reactor with nitrogen to 600

psig (41.8 atm), then slowly purging it. This sparging cycle was repeated ten times. Afterwards, the reactor was pressurized with nitrogen to an initial pressure of 40 psig (3.7 atm).

Table 2.1. Sulfur-containing compounds used.

General Compound Structure	Concentration Used (ppm, by mass S)
Mercaptan 1 (M1)	5000
Mercaptan 2 (M2)	5000
Aromatic sulfide (RS)	5000
Aromatic disulfide (RD)	5000
Aliphatic sulfide (LS)	5000
Aliphatic disulfide (LD)	5000
Cyclic thioether 1 (C1)	5000
Cyclic thioether 2 (C2)	5000

The reactors were heated using a Watlow 600 W sleeve heater by first wrapping the reactor in a thick layer of aluminium foil and sliding the sleeve heater over, to ensure a tight fit and thermal contact. The entire unit was then wrapped in a thermal blanket to insulate the unit and provide steady heating. Heating the reactors was controlled by an external power-supply, with feedback taken from a thermocouple placed inside the reactor. The heating rate was set to a constant 10 ºC/minute.

To analyze the thermal decomposition reactions the same experimental setup was used as with the corrosion experiments, with the exception that no metal coupons were placed in the cartridge heater alongside the sulfur compound. Therefore, during the course of the experiment the sulfur compound decomposed solely in the mineral oil. In these experiments a sample of the headspace gas was needed and extra care had to be taken not to release any gas from the reactor as the headspace gas was drawn out. To do this, 1 L Tedlar gas-sampling bag was first filled with 0.8 L of grade 4.8 argon. Then, a Swagelok rubber syringe unit was wrenched onto the valve of the sealed reactor containing the mineral oil and decomposed sulfur compound. Then, 20 mL of the headspace gas were slowly drawn out into a glass syringe as the valve was gently opened. This

sulfur-containing headspace gas was then mixed with the argon in the Tedlar sampling bag and analyzed for hydrogen sulfide (H_2S) by gas chromatography.

To look further into the reaction of H_2S with these metallurgies, all of the metals were also reacted under an atmosphere of H_2S at temperature. The metal wires were supported vertically with SEM mounting clips in a sealed tube-furnace, which was then fully sparged with argon. Afterwards, the furnace was filled with H_2S gas (5174 ppm H_2S, 10.19% hydrogen, argon balance), and this gas was continually flowing during the heat-up, reaction time, and cool down of the furnace. The furnace was brought to either a medium or medium-high temperature, and was held at temperature for either a quick, short, or long exposure time.

2-2: Steel Compositions

The metallurgies used and their compositions are shown in Table 2.2.

Table 2.2: List of metallurgies tested and their composition.

Metallurgy	Chromium (%)	Nickel (%)	Sulfur (%)	Carbon (%)	Molybdenum (%)
316 SS	16.0 - 18.0	10.0 – 14.0	0.030	0.08	2.00 – 3.00
410 SS	11.5 - 13.5	n/a	0.030	0.15	n/a
P91 (9Cr-1Mo)	8.00 - 10.0	n/a	0.025	0.15	0.9 – 1.10
5Cr	4.00 - 6.00	n/a	0.025	0.15	0.45 – 0.65
Carbon-steel	n/a	n/a	n/a	0.25	n/a

Alloy 410 stainless steel is a martensitic steel that is generally considered to be less corrosion resistant than the 300 series stainless steels. 316 stainless steel, also called 18-12 steel, is a common austenitic stainless steel usually used in power generation equipment, and has a higher creep strength than 304 stainless steel and is more heat resistant than 347 stainless steel.[41] P91 steel (also called 9Cr-1Mo-1W or E911) is popular for piping and tubing.[42] 5Cr steel (also called 5Cr-0.5Mo) reportedly has high strength and corrosion resistance against sulfur-containing crude oils, making it popular in the petroleum industry.[43] The metal samples used were in the form of extruded wire, with a diameter of 200 μm, and were cut into pieces 1-inch in length. Carbon-steel

was used to compare the effect of each sulfur compound under two different operating temperatures and two different experiment durations. The stainless steels and iron-chrome-molybdenum alloys were tested under the longest duration and highest temperature, to compare the effect of the sulfur compounds on each metallurgy under a uniform experimental setup. Table 2.3 presents a matrix showing the conditions of each experiment for each metallurgy, and which sulfur compounds were tested.

Table 2.3: Matrix of corrosion experiments performed.

Metallurgy	**Reaction Duration**	**Reaction Temperature**	**Sulfur Compound Tested**
316 SS	Long	Medium-High	All
410 SS	Long	Medium-High	All
P91	Long	Medium-High	All
5Cr	Long	Medium-High	All
Carbon-steel	Short	Medium	All
Carbon-steel	Short	Medium-High	All
Carbon-steel	Long	Medium	All
Carbon-steel	Long	Medium-High	All

All fouled wires were stored in air at room temperature prior to subsequent analysis, which included scanning electron microscopy (SEM), energy dispersive X-ray spectroscopy (EDXS), and X-ray diffraction (XRD). SEM and EDXS analysis utilized a Hitachi S-3000N microscope with an Oxford INCA EDXS system. The SEM was operated at an accelerating voltage of 15 kV, and a working distance ranging from 7-15 mm, for optimum resolution. EDXS scans were completed at a 15 kV accelerating voltage and a working distance of 15 mm. Cross sections of the wires were prepared by mounting a portion of each sample in a metallographic epoxy, to which a finely dispersed nickel powder was added to reduce charging. Subsequent, delicate grinding and polishing produced a cross sectional sample appropriate for imaging and analysis using SEM and EDXS. Thickness measurements of the rough, fouled wire surface were conducted as follows: Using Quartz PCI software the corrosion layer was measured radially at 8 places around the circumference of the wire cross section, in increments of 45°, starting at the 12 o'clock position.

XRD analysis was performed using a Bruker AXS D8 Discover diffractometer with a Histar GADDS area detector.

Chapter 3
Results

3-1: Compound Thermal Decomposition Studies, No Metals Reacted

Table 3.1 ranks the relative decomposition temperatures for each of the compounds tested in the reaction, without the presence of a metal wire or coupon to be corroded. It may be seen that there a distribution of decomposition stabilities in the examined compounds. For instance, the cyclic thioether compounds are highly stable far above their boiling points and the target corrosion temperatures. Meanwhile, the aliphatic disulfide readily decomposed in H_2S at temperatures below the corrosion temperatures.

Table 3.1: Temperature for initial H_2S detection after a long reaction time for each sulfur compound in mineral oil.

Sulfur Compound	**H_2S Initial Detection Temperature Ranking**
Aliphatic disulfide	Low temperature
Mercaptan 1, Mercaptan 2, Aromatic disulfide	Medium temperature
Aliphatic sulfide	Medium-high temperature
Aromatic sulfide, Cyclic thioether 1, Cyclic thioether 2	Not detected

From our decomposition experiments, neither cyclic thioether compound produced hydrogen sulfide gas at any experimental temperature provided. Cyclic thioethers are known to be relatively thermally stable molecules, even if they are in vapour form. For instance, authors have argued that the first step in the decomposition of a cyclic, aromatic compound such as thiophene is the breaking of C-S bond, which is expected to occur between 1026 ºC – 1076 ºC.[44] Alternatively, it has been argued that the decomposition reaction is started by the loss of hydrogen, which is the only bond dissociation to occur below 800 ºC.[45] Researchers contended that the breaking of the C-H bond in thiophene and other five-member rings require more energy than the dissociation of the C-H bond in six-member rings such as benzene.[46] Overall these earlier findings

fully agree with our observations that both cyclic thioethers would have highest hydrogen sulfide formation temperatures out of the tested lot. However, the exact products formed from the thermal decomposition of many cyclic thioethers can be solvent- and temperature-dependent.[47]

The mercaptans and aliphatic sulfide grouped closely with respect to hydrogen sulfide detection temperature, with the exception of the aliphatic disulfide, which formed hydrogen sulfide at a relatively much lower temperature than the others. The structure of each of these compounds appears to play a role in their decomposition temperature. This is supported by the work in ref.[48], in which a tert-structured alkanethiol produced sulfur and decomposed much more readily at a lower temperature than three n-structured alkanethiols. An iso-structured alkanethiol decomposed slightly more than any of the n-structured compounds, and less than the tert-structured compounds. This suggests that the S-S bond is comparatively weaker than any of the C-S bonds, and that both of these bonds are weaker than a C-C bond. It is known that the bond dissociation energy for a tertiary hydrogen is lower than that of a primary hydrogen,[49] which can suggest that any hydrogen in the system bonds with the free S molecules to form hydrogen sulfide, rather than bonding with a tertiary carbon.

The aromatic sulfides produced little or no hydrogen sulfide. Disulfides in general are fairly well-studied compounds, and it is known that the thermal degradation can usually begin with the cleavage of the S-S bond.[50] Authors found that sulfides can be formed as a product from the thermal degradation of disulfide,[51,52] with hydrogen sulfide as a product as well.[52] On the other hand, the aromatic sulfide compound tested turned out to be a fairly stable compound and hydrogen sulfide was not reliably detected from the decomposition of this compound at any temperature we provided in our experiments. The relative enthalpies between many aromatic sulfides and aliphatic sulfides can be researched.[53] The relative differences in these values can hint that although both

compounds are sulfides, the presence of aromatic groups stabilizes the overall structure more than the equivalent structure with an aliphatic groups.

In general, an approximate ranking system of hydrogen sulfide production from thermal decomposition of sulfur compounds can be established. The cyclic thioethers rank lowest and would decompose at the highest temperatures. For aliphatic sulfides and disulfides, the particular structure seems to generally correlate with decomposition temperature and hydrogen sulfide production. The tert- and iso- structured compounds decompose at lower temperatures and produce higher hydrogen sulfide concentrations than straight-chained alkanes. This trend is supported by the relatively low bond dissociation energy of both S-C bonds and S-H bonds compared to C-C bonds, and the reduced bond dissociation energy of tertiary hydrogens compared to primary or secondary hydrogens. Given a case of two compounds with similar structure, as was our case between aliphatic sulfide and aromatic sulfide and between aliphatic disulfide and aromatic disulfide, the presence of fairly stable aromatic-groups near the sulfur compound generally decreases the amount of hydrogen sulfide formed compared to counterpart compound containing an aliphatic-group.

3-2: Rectangular Coupons of Carbon-Steel

Preliminary work was performed on rectangular coupons of carbon-steel, with the later more-detailed experiments being performed on wires instead. The same 8 sulfur compounds were used for these experiments as with the decomposition experiments. The additive concentration was ppmmS (parts per million by mass S) was 5000, a medium reaction temperature was chosen, the starting pressure was 40 psig, the pressure at temperature was 60 – 80 psig, the coupon metallurgy was carbon-steel, and the oil type and volume tested was Paraflex HT-100, 9 mL. The number of

repetitions per experiment was 4, and no headspace analysis was performed for these specific specimens. A starting pressure of 40 psig was used. This is summarized in Table 3.2.

As will be demonstrated, the structure and the chemical stability of these molecules may be directly linked to aggressiveness in a corrosion environment.

Table 3.2: Table summarizing experimental conditions for experiments with carbon-steel coupons.

Compound	Temperature	Reaction Time	Pressure at Temperature (psig)
Mercaptan 1 (M1)	Medium	Short	60
Mercaptan 2 (M2)	Medium	Short	60
Aromatic sulfide (RS)	Medium	Short	63
Aromatic disulfide (RD)	Medium	Short	63
Aliphatic sulfide (LS)	Medium	Short	60
Aliphatic disulfide (LD)	Medium	Short	80
Cyclic thioether 1 (C1)	Medium	Short	63
Cyclic thioether 2 (C2)	Medium	Short	63

Figure 3.1 summarizes the experimental approach employed in this study. After testing, coupons were removed from the reactor, gently washed with xylene and IPA, and mounted in conductive epoxy (epoxy with nickel microparticles. In the cases where a large amount of corrosion product had delaminated into the oil, the flakes (powder) were collected via vacuum filtration for analysis. After mounting, the coupons were sectioned down the longitudinal axis using a metallography saw (wet cutting), and polished to P-4000 (5 micron) surface finish for observation (SiC polishing paper).

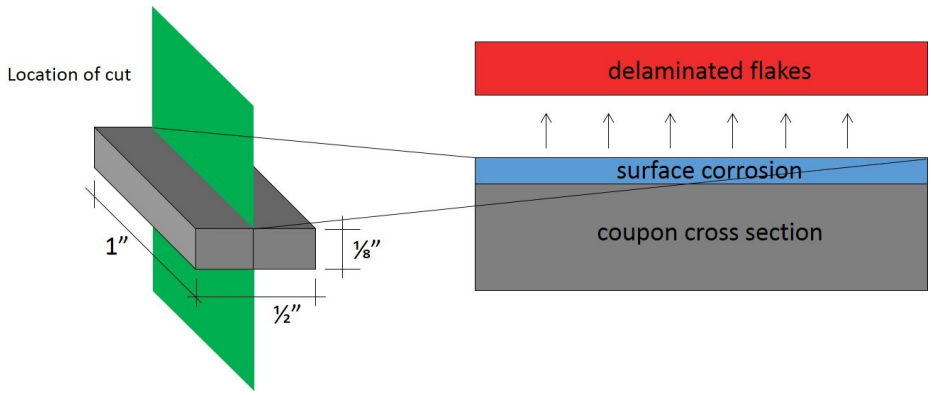

Figure 3.1: Experimental approach used for analysis of corroded coupons, showing how the coupon was cut as well as the surface corrosion and delaminated flakes.

Figure 3.2 shows the mean corrosion product thickness for each additive, obtained from cross sections of the tested coupons. It may be seen that there is a major difference in the corrosivity of each of the substances. Of course, without the additives there was no corrosion on the metal samples submerged in the Paraflex. In terms of additive corrosivity, the cyclic thioethers, C1 and C2, were the least corrosive. These molecules are known to be highly stable and would not be expected to decompose at a medium temperature although they would be present as a gas phase rather than a liquid. The aliphatic and highly thermally unstable mercaptans, M1 and M2, were the most corrosive, generating a 12 – 14 micron thick layer of a corrosion product on the metal surface for the duration of the experiment. The aliphatic sulfide and aliphatic disulfide species, labelled LS and LD, respectively, both generated approximately 11 microns of corrosion product. The aromatic sulfide, labelled RS, generated approximately 5 microns, while the aromatic disulfide, labelled RD, produced a 2 micron thick corrosion product.

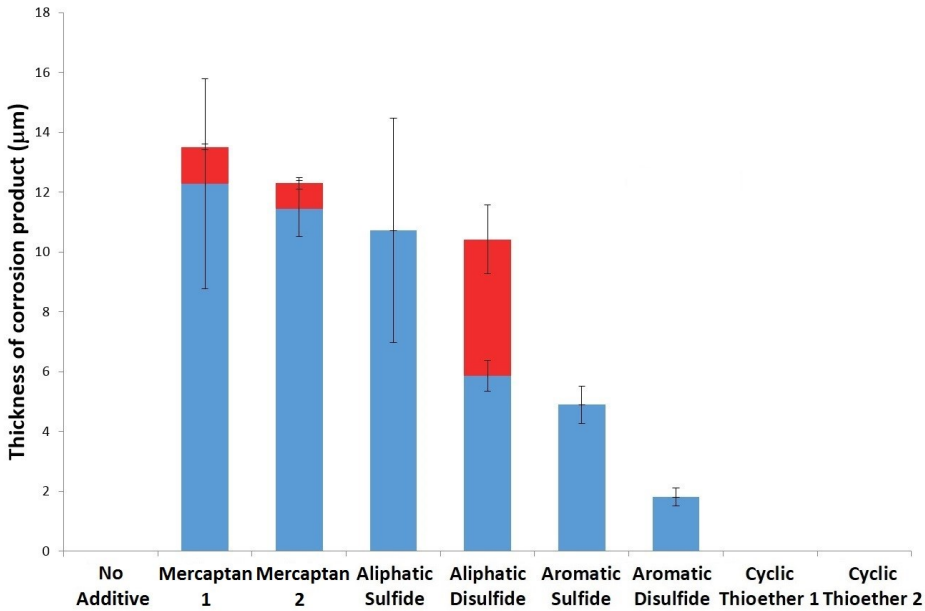

Figure 3.2: Thickness of the corrosion product on each carbon – steel coupon. Red regions indicated delaminated corrosion product, while blue regions indicate surface corrosion.

Figure 3.3 shows SEM micrographs of polished carbon-steel coupon cross-sections, comparing the effects of each compound on surface corrosion. Nickel particle infused mounting

epoxy is visible in the right half of all micrographs and marks the corrosion layer –epoxy boundary. The sequence of corrosion layer thickness is described in the previous figure. What this series of images illustrates is the overall corrosion layer morphology as a function of additive.

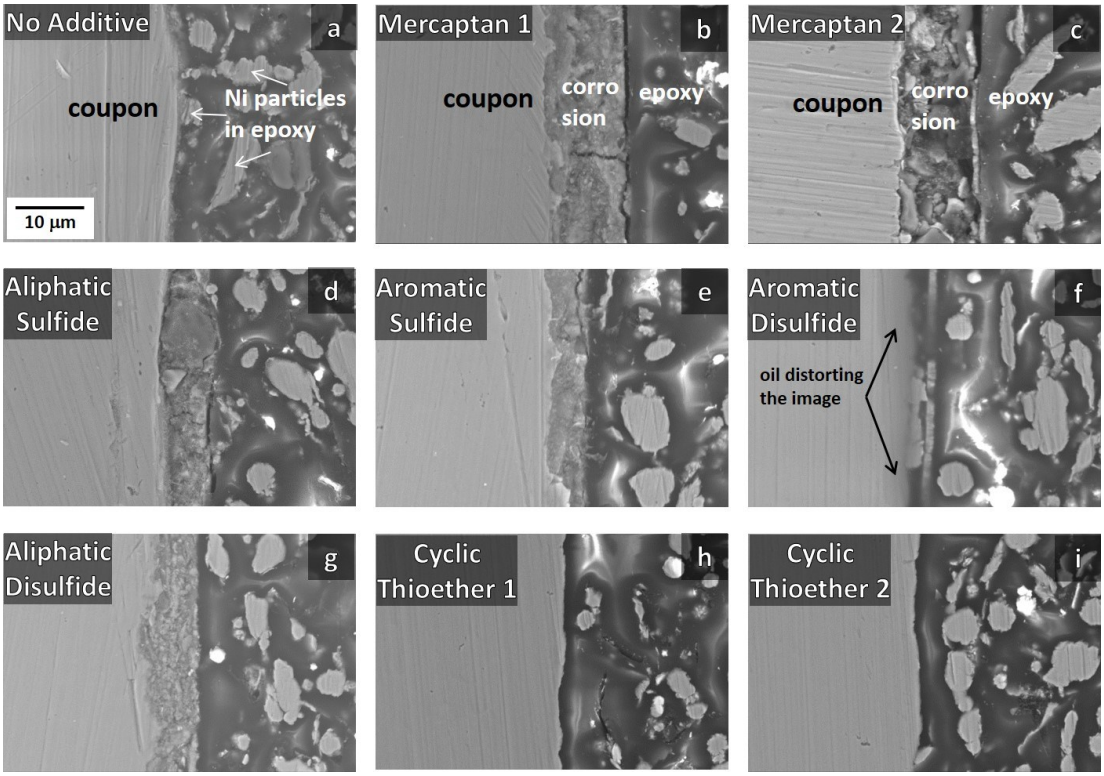

Figure 3.3: SEM micrographs of polished carbon-steel coupon cross sections, comparing the effects of each compound on surface corrosion. Nickel particle infused mounting epoxy is visible in the right half of all micrographs and marks the foulant –epoxy boundary.

The coupon surfaces with no additive (a), cyclic thioether 1 (h) and cyclic thioether 2 (i) are effectively pristine. The epoxy and the Ni particles contact the metal surfaces directly, with no corrosion product being detected. In fact all three metal surfaces still show the surface deformed layer associated with the manufacturing process. The aromatic disulfide (f) shows a fairly thin corrosion product, which tends to easily spall from the metal surface. The more corrosive species all tend to attack the metal surface relatively non-uniformly, with noticeably thicker and thinner regions being detected in all specimens. The morphology of the corrosion layer is highly

heterogeneous, and will be demonstrated to consist of a porous iron sulfide of varying grain sizes and crystallite morphologies.

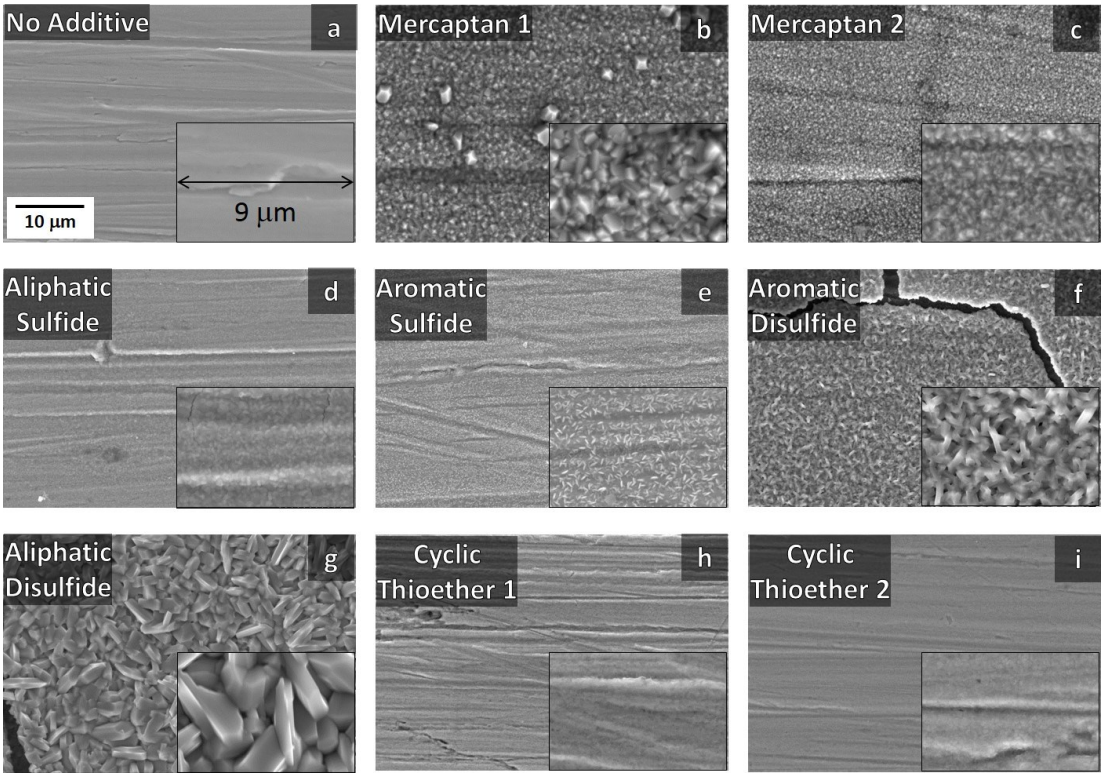

Figure 3.4: SEM micrographs of carbon-steel coupon surfaces after treatment with sulfur compounds. The inset micrographs are 9 μm wide.

Figure 3.4 shows the SEM micrographs of carbon-steel coupon surfaces after treatment with sulfur compounds. The inset micrographs are 9 μm wide. It may be seen from the plan-view morphology of the corrosion layers that the corrosion layer due to the aliphatic disulfide has larger crystallite size than the other specimens. Interestingly, this does not appear to translate to an overall thicker morphology of the foulant, and implies that there may be some differences in the mechanisms of the layer growth from compound to compound. The corrosion layer is iron sulfide and the larger crystallite size may imply a lower initial nucleation rate as compared to the finer grained sulfides found with other precursors. More work however is needed to conclusively elucidate the phenomenology of the growth kinetics in each system.

Figure 3.5 shows high magnification SEM micrographs and accompanying EDXS line scans of the corrosion products. Figure 3.5(a) shows the results with M1, (b) M2, (c) LS, and (d) LD. In all cases the corrosion product may be seen as being S and Fe- rich, being confirmed in later studies to be iron sulfide. There is some iron oxide present in the corrosion product as well. Since the oil was sparged with nitrogen prior to testing, it is highly likely that the rust was formed after the experiments, while the samples were being polished. We cannot rule out slight variations in polishing and drying as being responsible for the sample-to-sample difference in the rust content. Conversely, the samples which do demonstrate more non-uniform sulfidic attack do seem to be more susceptible to surface oxidation, which may reasonable considering that a microscopically rough surface that is partially sulfided could rust faster.

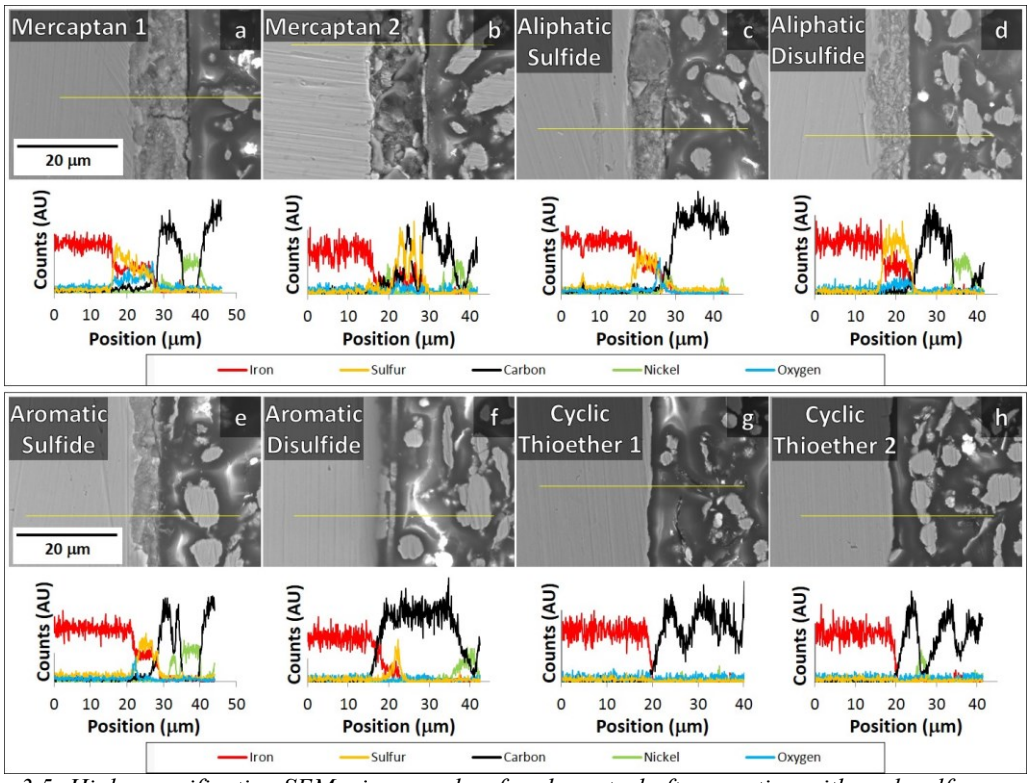

Figure 3.5: High magnification SEM micrographs of carbon-steel after reacting with each sulfur compound for 4 hours. EDX line scans are shown under each micrograph.

Figure 3.6 shows SEM micrographs of the corrosion product flakes that came off of the carbon-steel coupons treated with the aliphatic disulfide. A portion of the deposit appears to have

delaminated during the experiment, exposing a fresh metal underneath to more sulfidic attack. This caused a secondary sulfidic film to nucleate on the metal surface, with a physical gap between the first and the second corrosion layer. This is shown in Figure 3.6(a). The surface of the film shows evidence of compressive stress resulting in film buckling and delamination, as shown in Figure 3.6(b). As may be seen in Figure 3.6(c), the underside of a corrosion-product flake shows what appears to be preferential sulfidic attack at the carbon-steel grain boundaries. The corrosion product surface being imaged would be adjacent to the carbon-steel surface.

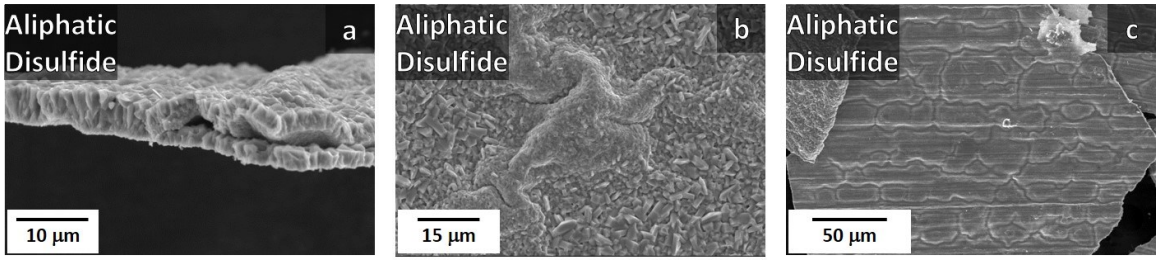

Figure 3.6: SEM micrographs of the corrosion product flakes that came off of the carbon-steel coupons treated with the aliphatic disulfide. (a) A portion of the deposit appears to have delaminated approximately half-way through the run and exposed fresh metal underneath, allowing the reaction to continue. (b) Surface of the film showing evidence of compressive stress resulting in film buckling and delamination. (c) Underside of the flake showing what appears to be preferential sulfidic attack at the carbon steel grain boundaries. This surface would be adjacent to the carbon steel surface.

3-3: Wire Cross-Sections of Carbon-Steel

For the remaining experiments we switched from rectangular coupons to 200 µm diameter wires of the same metallurgy. This eliminated the observed variation in corrosion attack with positions in the specimens (e.g. coupon edge vs. flat section) and gave overall substantially more uniform results. The key experimental parameters are summarized in Table 3.3, with each run being repeated 4 times, headspace analysis being performed in each case, and the starting pressure being 40 psig.

Figure 3.7 shows SEM cross-sections of carbon-steel wires reacted with each sulfur compound under four different conditions created with two temperatures (medium and medium-high) and two experiment durations (referred to as short and long). The no-additive experiments

shown in 3.7(a) show that the wires emerge from plain mineral oil practically unreacted. One general trend observed is that the level of hydrogen sulfide production and decomposition temperature correlates fairly well with the amount of corrosion on each sample.

Table 3.3: Summary of experimental conditions for corrosion experiments involving carbon-steel wires at all temperatures and time durations.

Compound	Temperature	Time	Pressure at Med/Med-High (psig)
Mercaptan 1 (M1)	Med/Med-High	Short/Long	60/80
Mercaptan 2 (M2)	Med/Med-High	Short/Long	60/80
Aromatic sulfide (RS)	Med/Med-High	Short/Long	63/80
Aromatic disulfide (RD)	Med/Med-High	Short/Long	63/80
Aliphatic sulfide (LS)	Med/Med-High	Short/Long	60/80
Aliphatic disulfide (LD)	Med/Med-High	Short/Long	80/90
Cyclic thioether 1 (C1)	Med/Med-High	Short/Long	63/80
Cyclic thioether 2 (C2)	Med/Med-High	Short/Long	63/80

The effect of temperature and reaction time are evident in 3.7(d), for example, which shows that the reactions with aliphatic sulfide created thicker sulfide layers as temperature and time increased. Figures 3.7(h) and (i) show the carbon-steel samples reacted with the two cyclic thioethers, and as with the metal coupons they were effectively pristine after these reactions.

Figure 3.7(d) depicts the results from the aliphatic sulfide compound, which correlate very well with our decomposition experiments. This compound was found to decompose into hydrogen sulfide fairly readily, and the corrosion experiments performed at medium heat for both time lengths show negligible corrosion. However, at medium-high heat, the iron sulfide layer grew considerably between the short and long experiment runtimes. These results correlate well with Figure 3.9, which show that when reacted at medium-high heat for a short length of time, a small but measureable amount of hydrogen sulfide formed. When reacted at medium-high heat for a long length of time, a substantially larger amount of hydrogen sulfide formed, suggesting that it played a role in the increased corrosion.

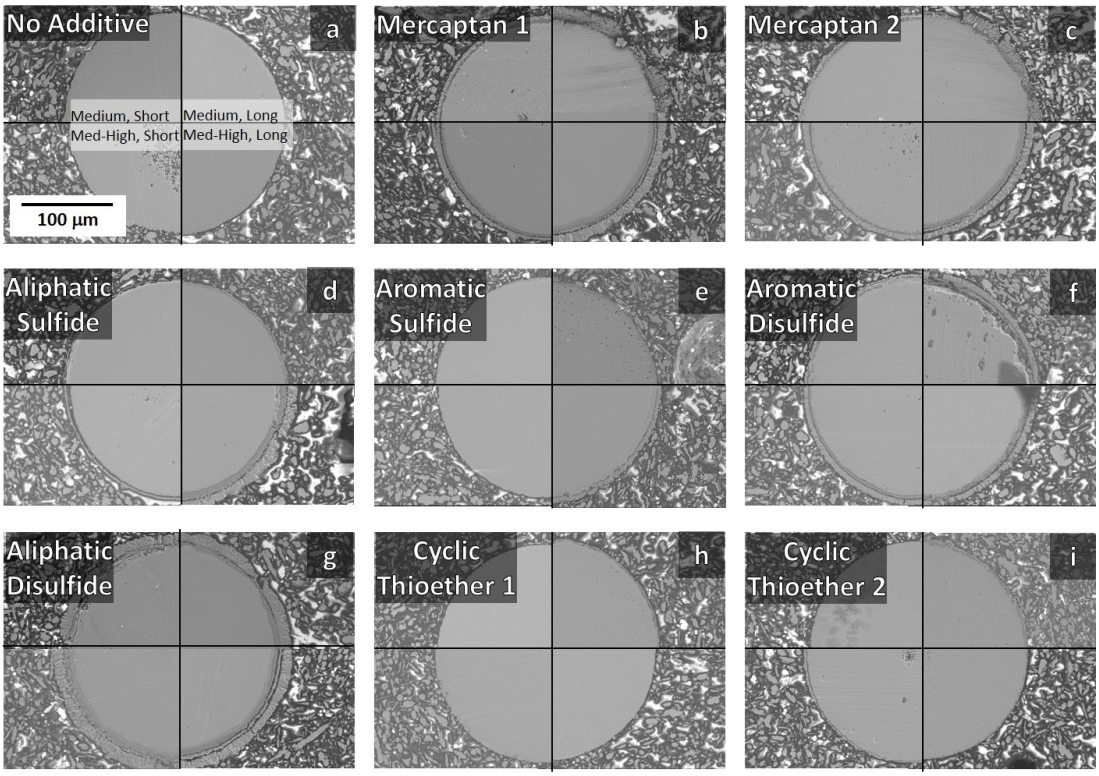

Figure 3.7: SEM micrographs of polished carbon-steel wire cross sections, comparing the effects of each compound on surface corrosion. Quadrants in each sub-figure show either medium or medium-high temperature, reacted for either a short or a long time-period. Nickel particle infused mounting epoxy is visible surrounding each wire cross section.

Figures 3.7(b) and (c) show the two mercaptans, M1 and M2, respectively. When reacted at medium-high heat for a long length of time these compounds produced thick iron sulfide corrosion layers and relatively large amounts of hydrogen sulfide, as shown in Figures 3.9 and 3.10. However, at the other three reaction conditions no hydrogen sulfide formed, yet a measurable iron sulfide layer still formed. In some cases the sulfide layer thickness was the second thickest layer observed. These results imply that a corrosion mechanism involving mercaptans does not necessarily depend on a formation of hydrogen sulfide.

Figure 3.7(f) shows the results of the aromatic disulfide compound. All the conditions tested showed that a fairly moderate iron sulfide layer formed when carbon-steel was reacted with this compound. Despite our experiments showing that this compound decomposed and formed hydrogen sulfide at the same temperature as the mercaptans, only a small amount of hydrogen

sulfide was found during the experiments with carbon-steel only at medium-high heat for a long length of time. This may imply that the hydrogen sulfide was consumed during the corrosion process which created the thick corrosion layers.

The results of the aromatic sulfide shown in Figure 3.7(e), and of the cyclic thioethers C1 and C2 in Figures 3.7(h) and (i), respectively, show very similar trends. First, none of these compounds decomposed into H_2S in our thermal decomposition experiments. Second, none of these compounds produced hydrogen sulfide when reacted with carbon-steel at any of the experimental conditions. The structure of the surface corrosion in each case is quite different, however. Figures 3.8(h) and (i) show the surface SEM micrographs the C1 and C2 samples to be very similar to the no-additive samples. The lack of clear crystal growth on these samples is contrasted with the surface micrographs of the aromatic sulfide, shown in Figure 3.8(e).

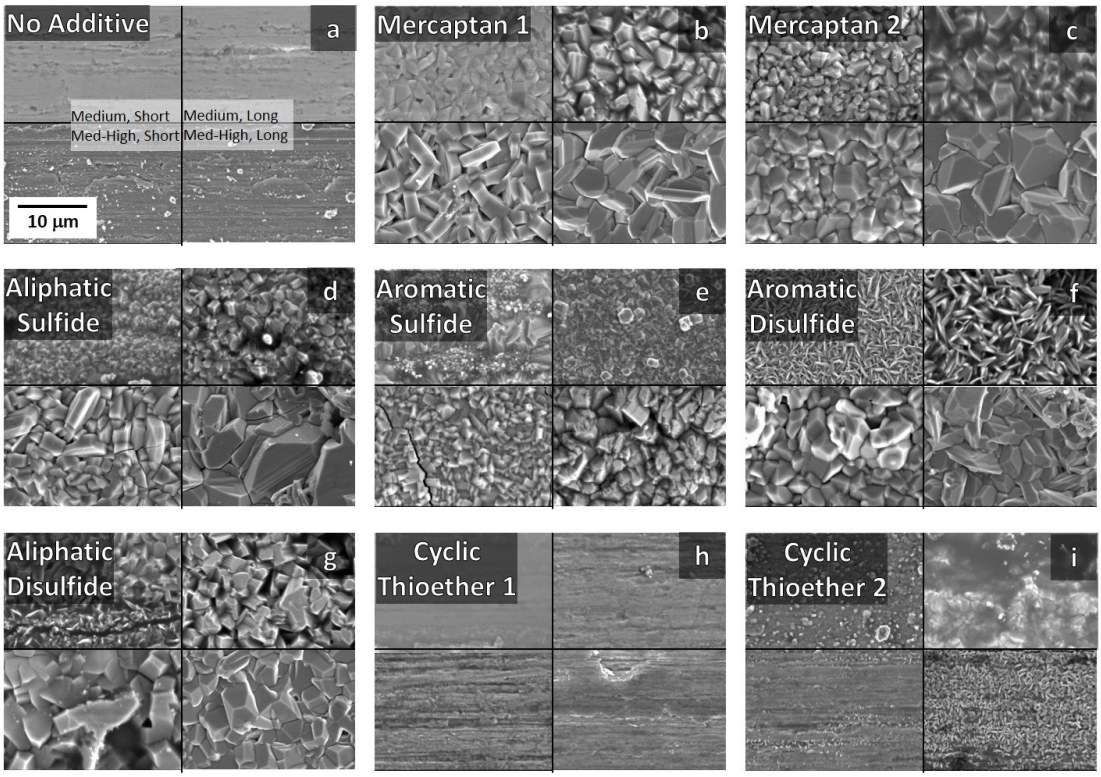

Figure 3.8: SEM micrographs of carbon-steel wire surfaces after treatment with sulfur compounds. Quadrants in each sub-figure show either medium or medium-high temperature, reacted for either a short or a long time-period.

Figure 3.8 shows the SEM micrographs of carbon-steel surfaces. In general, increasing the experiment duration increased the crystal size. Changing the temperature, however, had the potential to change the predominant crystal shape, an effect seen in 3.8(f) with the aromatic disulfide. Overall, the largest crystals were seen with the reactions at medium-high heat, held for a long length of time.

Figure 3.9 shows the amount of hydrogen sulfide produced during each reaction, and clearly shows that under all four reaction conditions the aliphatic disulfide produced relatively large amounts of hydrogen sulfide gas. The cyclic thioethers C1 and C2 did not decompose into any measured hydrogen sulfide gas during any experiments. In general, hydrogen sulfide was only detected when the reactions were done at medium-high heat and held there for a long length of time. The distinct difference between headspace H_2S detected without (Table 3.1) and with the corroding wires in the reactor indicate that much of the H_2S generated is consumed by the reaction to form the sulfide. Presumably in the cases where H_2S is detected with the wires present, there is such copious amount that is given off that not all of it is consumed.

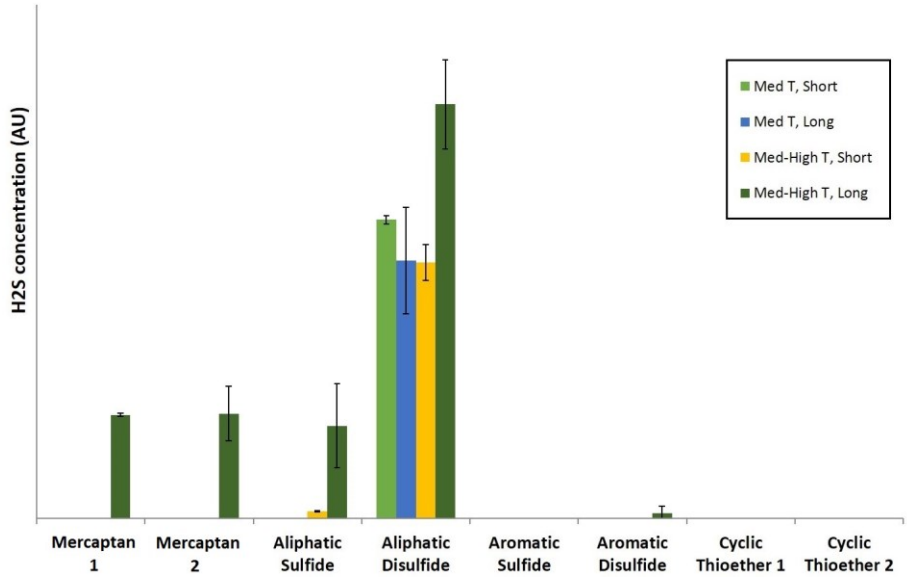

Figure 3.9: Relative measure of hydrogen sulfide formed during the reaction of each sulfur compound with carbon-steel at all tested conditions.

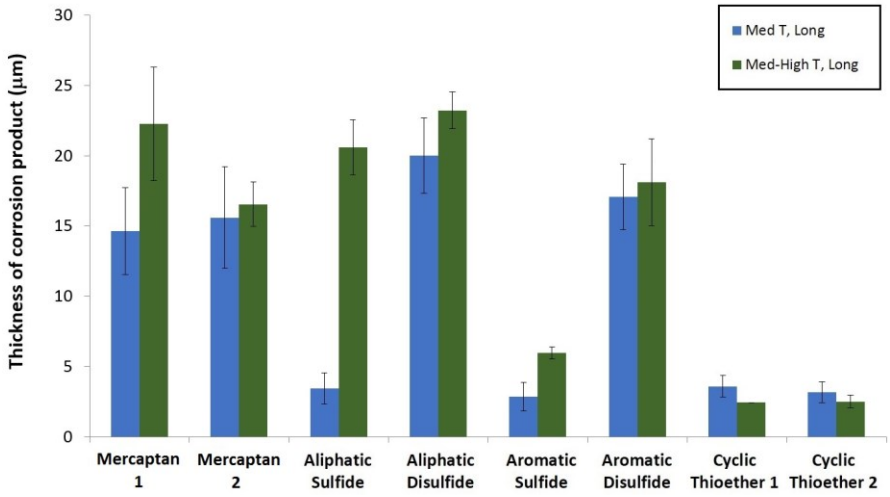

Figure 3.10(A): Measured thickness of corrosion product in micrometers for carbon-steel and each sulfur compound, for long reaction times at both system temperatures.

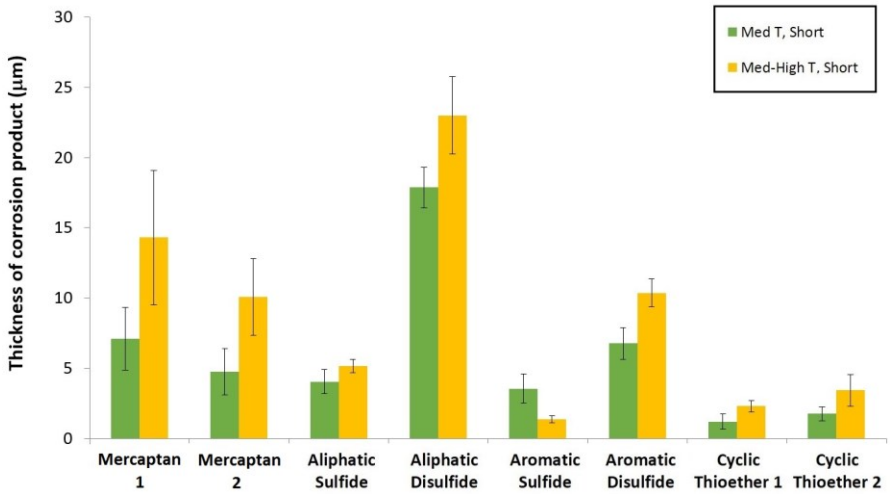

Figure 3.10(B): Measured thickness of corrosion product in micrometers for carbon-steel and each sulfur compound, for short reaction times at both system temperatures.

Figures 3.10(A) and 3.10(B) quantify the surface corrosion by plotting the thickness of the corrosion product created with each compound after being reacted for either a long or short length of time, respectively. For the aliphatic disulfide, the two cyclic thioethers, and the aromatic sulfide, the results are relatively intuitive. Only minor levels of corrosion occurred at either reaction temperature, as these latter three molecules did not decompose into H_2S readily. Conversely, the aliphatic disulfide molecule is completely decomposed at the medium reaction temperature,

leading to the highest H_2S corrosion rates observed for this temperature range. Interesting and more complex results are for the mercaptans M1 and M2, and the aromatic disulfide RD, which all decomposed at the same temperature, and the aliphatic sulfide LS, which decomposed at a slightly higher temperature. We focus on the long reaction time data, rather than short reaction time corrosion data, since it goes beyond the early-stage variations in kinetics to show the longer-term corrosion trends that are more meaningful to practical refinery operations. What is observed is that a direct correlation between the decomposition temperature and the amount of corrosive product. The aliphatic sulfide compound tested serves as the key case for this argument. At medium temperatures the compound is stable and fairly minor corrosion occurs, effectively on par with what is observed with the cyclic thioethers. Conversely, the medium-high temperature is above the decomposition temperature for this compound, with the subsequent degree of corrosion being quite on par with the other four compounds that are decomposed at the medium-high temperature. It can be argued that two mercaptans M1 and M2, and aromatic disulfide RD, are at the onset of decomposition at the medium reaction temperature, explaining why at that temperature their corrosion levels are intermediate between those corresponding to fully stable and fully unstable compounds.

Overall the data seems to fall in three blocks: Most corrosion occurs when the compounds are fully decomposed to H_2S, intermediate corrosion occurs when the compounds are tested at temperatures right near the onset of decomposition, and least corrosion occurs when the compounds are stable. While there is some compound-to-compound variation within these three bands, the above trend is quite conclusive. It is interesting to note that although the amount of corrosion is substantially lower at temperatures where the compounds are stable, it is not nil. This indicates that there is a certain intrinsic corrosiveness of the tested sulfur compounds per se. The

short reaction time data is generally much less conclusive, and there is likely a kinetic effect associated with limited rates of compound decomposition at either temperature and perhaps more significantly differences in the initial corrosion kinetics from compound-to-compound.

Figures 3.11-3.14 display the high magnification SEM micrographs of carbon-steel samples reacted with each sulfur compound under the four experimental conditions, along with its accompanying EDXS line scan below each micrograph.

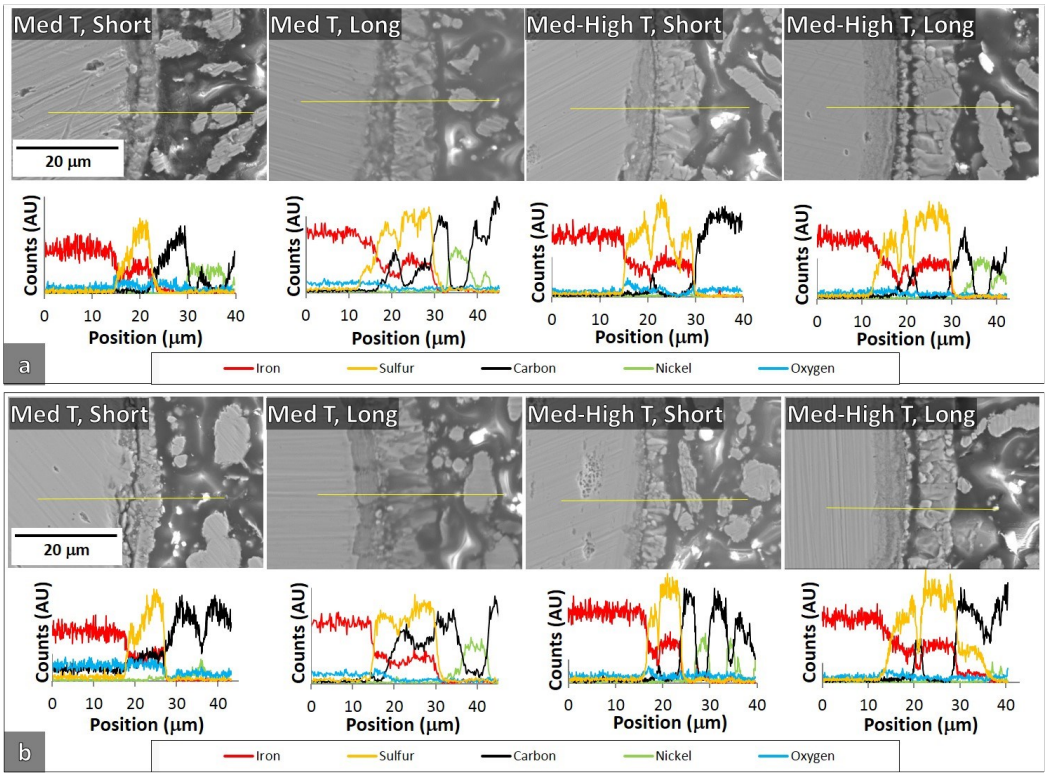

Figure 3.11: SEM micrographs of carbon-steel reacting for indicated temperatures and times with sulfur compounds: (a) mercaptan 1, and (b) mercaptan 2.

Figures 3.11(a) and (b) present the results of the mercaptan M1 and M2, respectively. Figure 3.12 presents (a) the aliphatic sulfide and (b) the aliphatic disulfide. The micrographs in 3.12(b) illustrate the corrosivity of the aliphatic disulfide, where a thick corrosion layer formed at all times/temperatures.

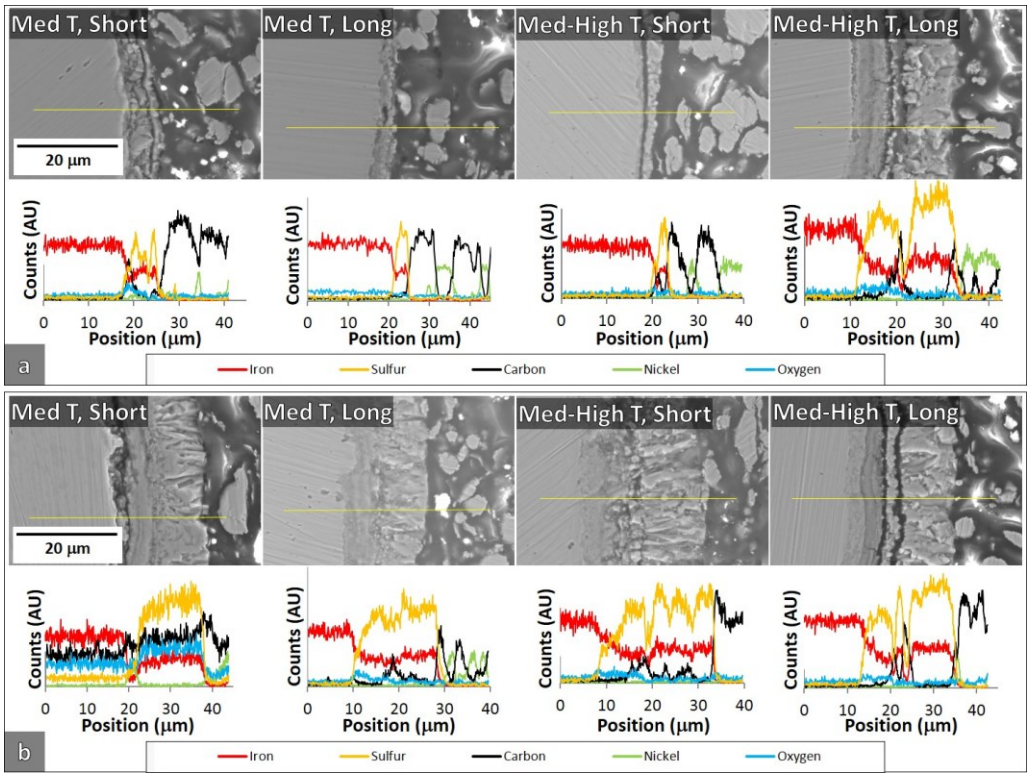

Figure 3.12: SEM micrographs of carbon-steel reacting for indicated temperatures and times with sulfur compounds: (a) aliphatic sulfide, and (b) aliphatic disulfide.

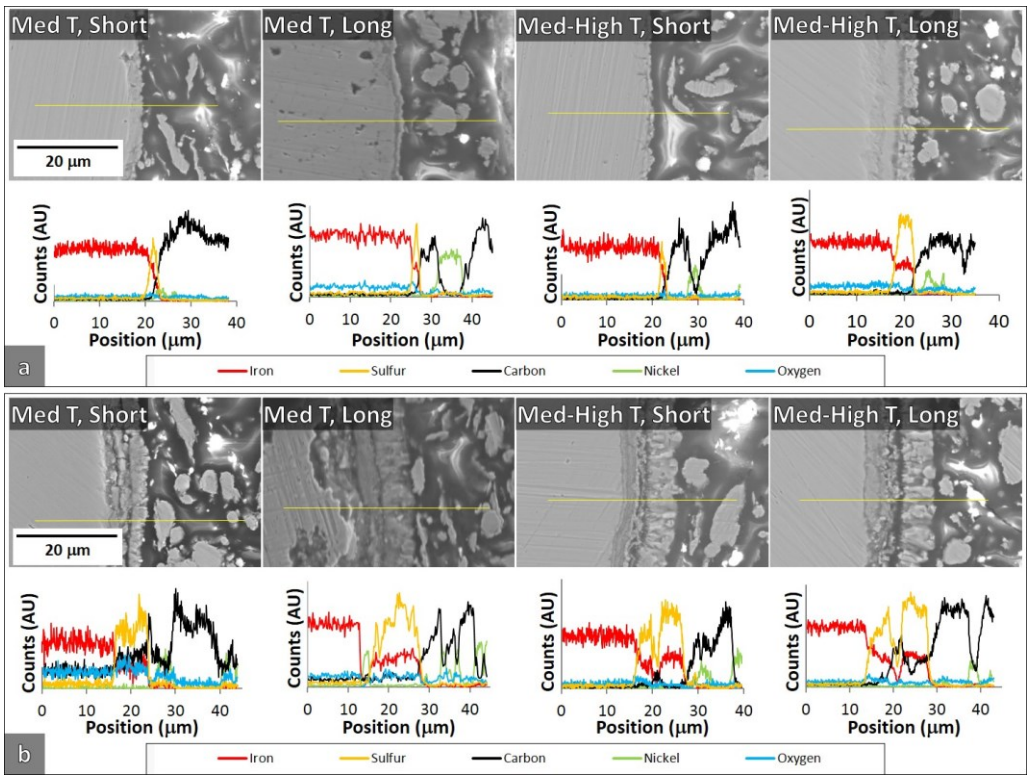

Figure 3.13: SEM micrographs of carbon-steel reacting for indicated temperatures and times with sulfur compounds: (a) aromatic sulfide, and (b) aromatic disulfide.

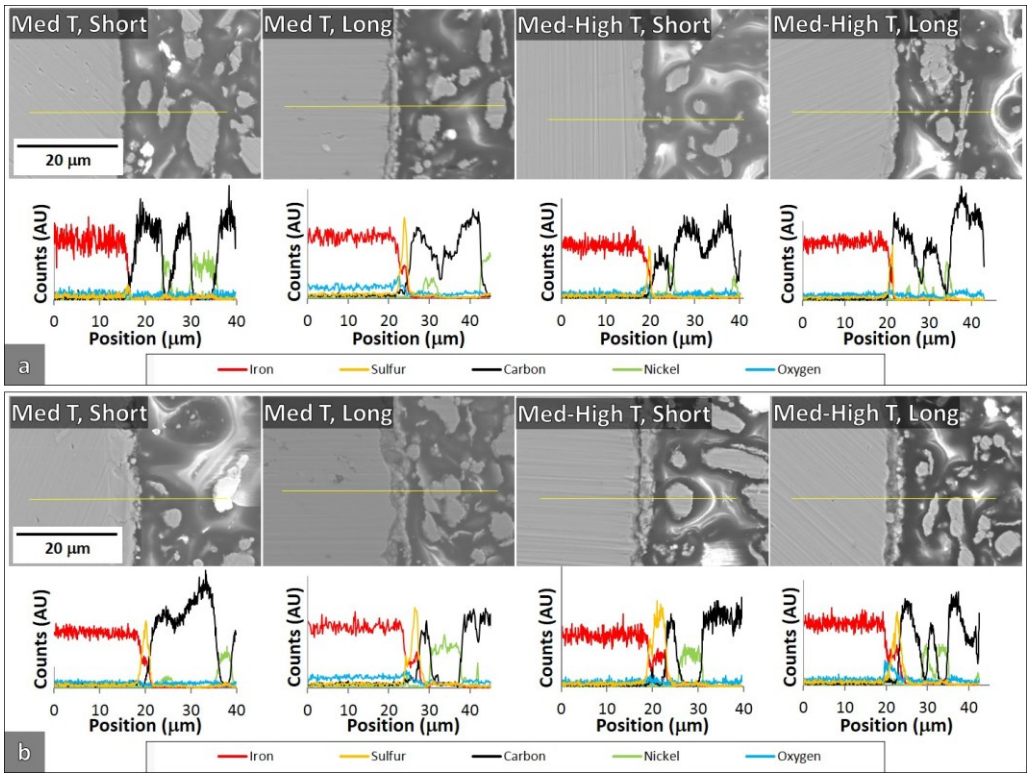

Figure 3.14: SEM micrographs of carbon-steel reacting for indicated temperatures and times with sulfur compounds: (a) cyclic thioether 1, and (b) cyclic thioether 2.

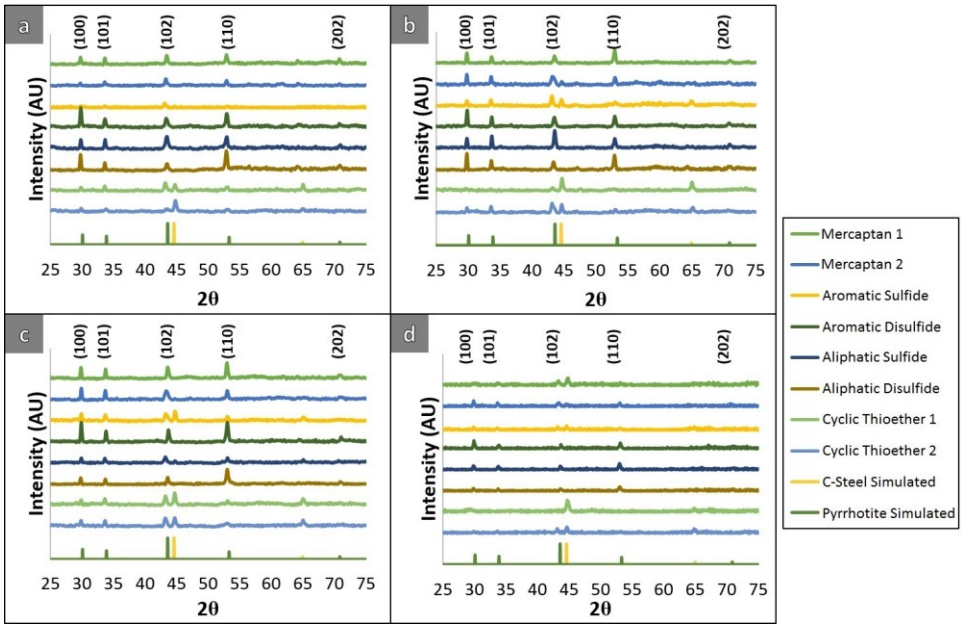

Figure 3.15: Master plot of all XRD scans of carbon-steel wires with each sulfur compound. (a) Medium-high temp. for long reaction. (b) Medium-high temp. for short reaction. (c) Medium temp. for long reaction. (d) Medium temp. for short reaction.

For contrast, Figure 3.13(a) shows the results of the aromatic sulfide. This species was not particularly reactive or corrosive, and even at the highest temperature and longest duration only a

thin corrosion layer formed. However, in all cases its corrosivity increased with temperature, producing a sulfur-rich corrosion layer. The two cyclic thioethers C1 and C2, shown in Figure 3.14(a) and (b), respectively, were largely unreactive with the carbon-steel samples. There was only a very thin corrosion product layer formed. It was present only in isolated sections of the wire surface, rather than as a continuous sheath.

Figure 3.15 shows a master plot of the XRD results for all of the carbon-steel specimens. The steel itself possesses a strong (110) texture, corresponding to the single visible bcc peak at $2\theta = 44.6°$ in the simulation and in the patterns of the weakly corroded specimens, such as the cyclic thioethers. The samples which do undergo sulfidic corrosion all show the presence of P-pyrrhotite, (P6(3)/mmc $Fe_{(1-x)}S$, which is isostructural with FeS triolite. The key XRD peaks are slightly shifted from their ideal locations for each specimen, which may be due to one or a combination of strain in the corrosion product and variations in stoichiometry. The XRD pattern for triolite would look identical P-pyrrhotite except for minute and uniform shifts in the peak positions to smaller 2θ values, i.e. a slightly larger lattice parameter of the former. Thus its presence cannot be ruled out, as it would be formed via an identical sulfiding mechanism. Overall despite an initial major difference in the types of compounds employed and the morphology of the corrosion products, the actual resultant phases appear analogous for each test condition.

3-4: Effect of Metallurgy and Sulfur Compounds at Constant Exposure

Four different metallurgies, also in the form of extruded wire, were studied in addition to carbon-steel: 316 stainless steel, alloy 410 stainless steel, P91 steel, and 5Cr steel. Each of these metallurgies were reacted with each of the eight sulfur compounds. In all cases the reaction conditions were set to the long reaction time at the the medium-high temperature. The 316 stainless steel had the highest chromium content of these metallurgies, which led to the prediction that this

steel would corrode the least. Figure 3.16 shows a series of micrograph cross sections of each metallurgy reacted with each compound. The only compounds that measurably corroded the 316 steel were the aromatic disulfide and the aliphatic disulfide, shown in Figures 3.16(f) and (g), respectively. The overall corrosion layer thickness from these two compounds were similar, yet the aromatic disulfide formed much less hydrogen sulfide. This indicates that the corrosion of 316 SS is not as dependent on a hydrogen sulfide pathway as was observed for the carbon-steel metallurgy. Figure 3.17 shows the corresponding SEM micrographs of the metallurgy surfaces with each of the sulfur compounds.

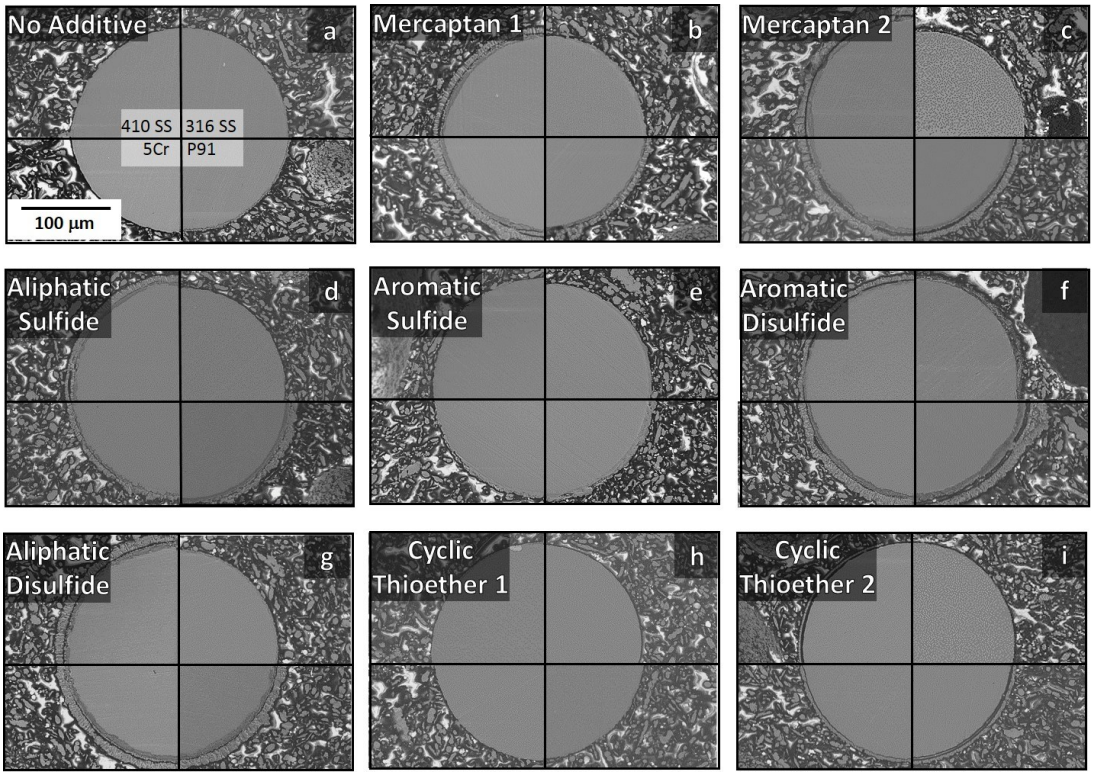

Figure 3.16: SEM cross-sections of all sulfide reactions. In each sub-figure the metallurgies are presented, from top-left going clockwise, as: 410SS, 316SS, P91, 5Cr.

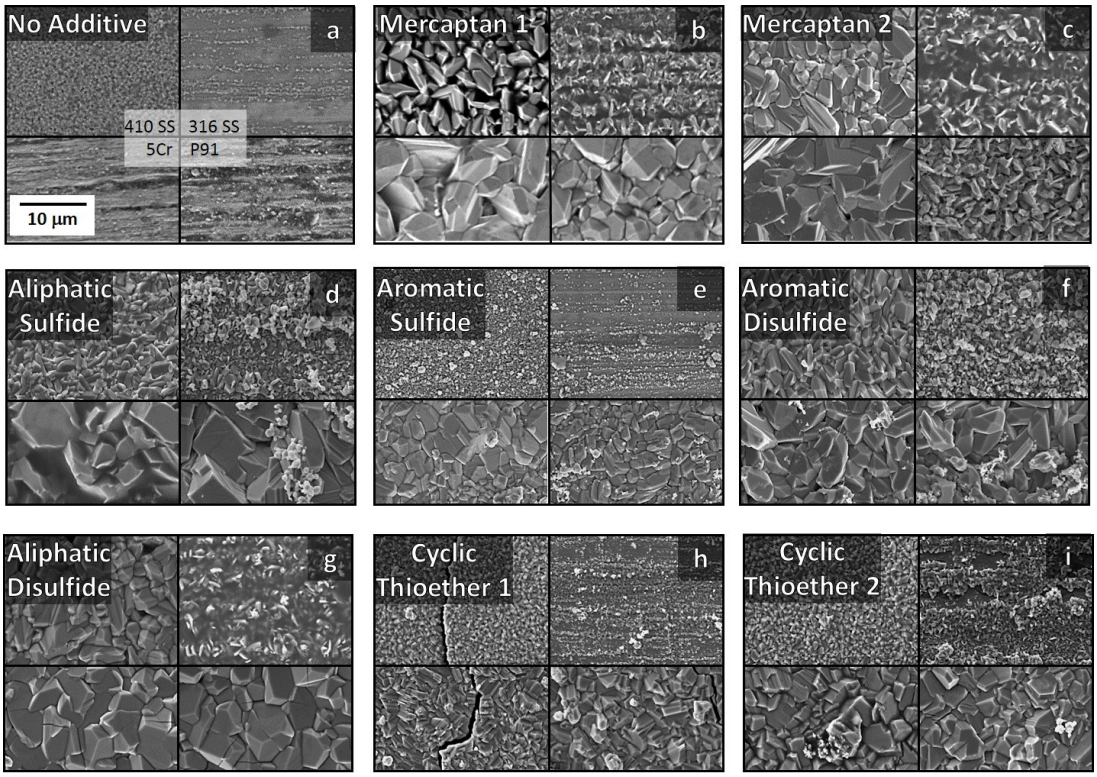

Figure 3.17: SEM surface micrographs of all sulfide reactions. In each sub-figure the metallurgies are presented, from top-left going clockwise, as: 410SS, 316SS, P91, 5Cr.

Figure 3.18(A) shows the amount of H_2S evolved from the carbon-steel, the P91 and 5Cr metallurgies, all tests being carried out at the medium-high temperature for a long reaction time. These trends are quite analogous for all three non-stainless metallurgies: The aliphatic disulfide evolves copious H_2S at temperature, while the mercaptans and the aliphatic sulfide evolve intermediate amounts of H_2S, and finally the aromatic sulfide and the cyclic thioethers evolve minimal H_2S. The data for aromatic disulfide is difficult to interpret since the compound on carbon-steel seems not to decompose at temperature, whereas it decomposes to a significant extent when in contact with the 5C and P91. More work is needed to investigate the source of this discrepancy, which may be due to a range of factors including the differences in the H_2S corrosion susceptibility of the three alloys and/or the differences in the catalytic efficacy of the three metal surfaces in driving the decomposition of the molecule.

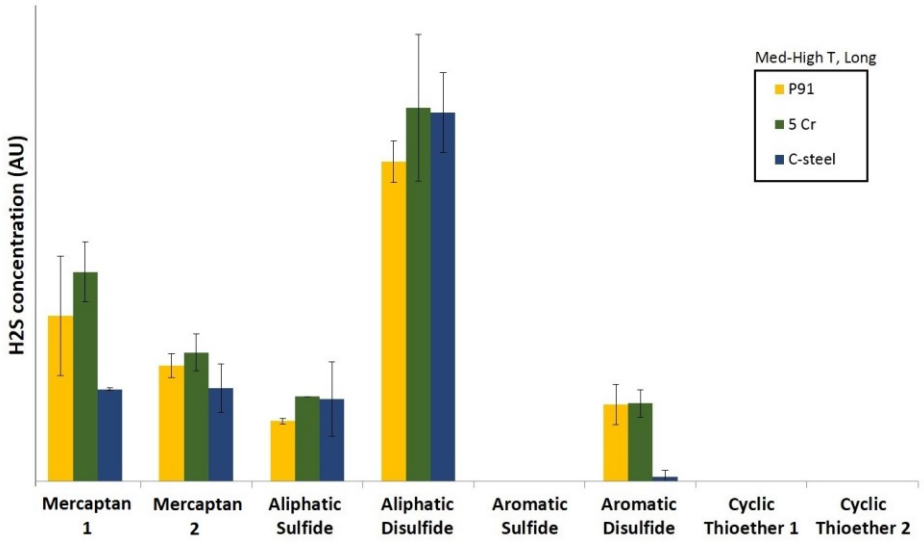

Figure 3.18(A): Relative measure of hydrogen sulfide produced for each sulfur compound, with P91, 5Cr, and carbon steel at medium-high temperature, for a long reaction time.

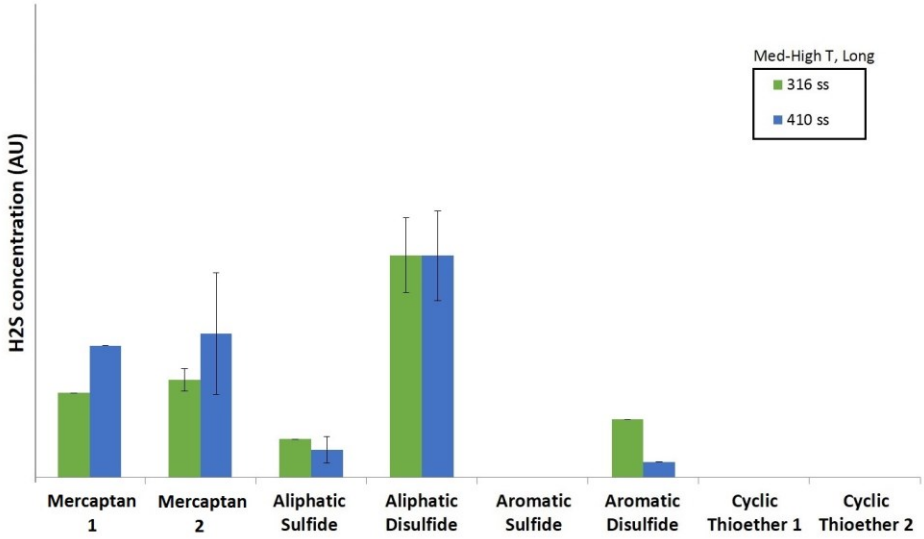

Figure 3.18(B): Relative measure of hydrogen sulfide produced for each sulfur compound, with 316SS and 410SS at medium-high temperature, for a long reaction time.

As well, it is likely that the surface metallurgy does indeed have a catalytic role in driving the dissociation of all these species. This is supported by the lower levels of H_2S evolved on 316 and on 410, whose surfaces are nominally covered by protective Cr – oxides. Consider the case of the aliphatic disulfide, which is both the least stable compound and the most corrosive. Of all the metallurgies, 316 stainless is by far the most corrosion resistant. Thus when 316 is exposed to the aliphatic disulfide at the medium-high temperature for the long reaction time, one would expect

the least amount of the decomposition product H_2S to be tied up as a corrosion product FeS. If this compound's decomposition was not catalytically driven, one would thus expect to measure the most H_2S in the headspace analysis when the 316 wires were present in the reactor. Yet in fact, the case is opposite, with the 316 and 410 samples generating less H_2S compared to that formed with the carbon-steel and 5Cr samples. While there is some scatter in the trends observed with the other H_2S generating species, one can argue for a trend that both stainless steels lead to less H_2S generation than their non-stainless counterparts.

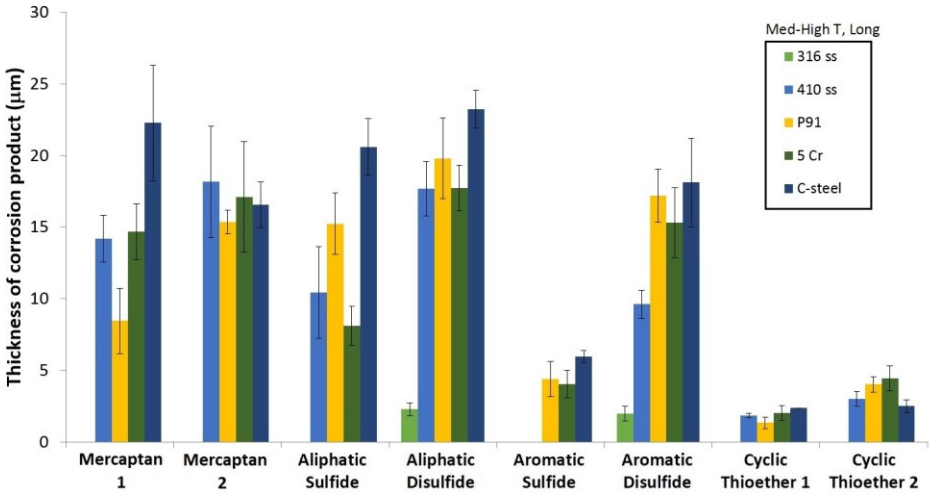

Figure 3.19: Thickness of the corrosion product formed on each metallurgy, for each sulfur compound, reacted at medium-high temperature, for a long reaction time.

Figure 3.19 shows the thickness of the corrosion product formed for all the metallurgies examined. Overall the C steel does appear to be somewhat less corrosion resistant than the other metallurgies, although the trend is not very strong. Interestingly, while there are variation from compound to compound, in general the 410 stainless, the P91, and the 5Cr appear on-par as far as their corrosion resistance. In fact, with the mercaptans M1 and M2, the non-stainless P91 actually outperforms stainless 410. The 316 stainless is by far the most stable against corrosion by any of the species tested, being clearly superior to 410.

Figures 3.20 – 3.23 show a series of SEM cross-sections with the accompanying EDXS analysis, of all the corroded metallurgies. These highlight a rich distribution of sulfide corrosion product morphologies formed across the metallurgy and compound types. In general, not only is the thickness of the sulfide different for each metal and compound combination, but so is the size and morphology of the sulfide crystals as well as their packing density and porosity. Moreover the microstructure within a given corrosion product is highly heterogeneous; the sulfides present at the metal interface are quite distinct from the sulfides present near the oil interface.

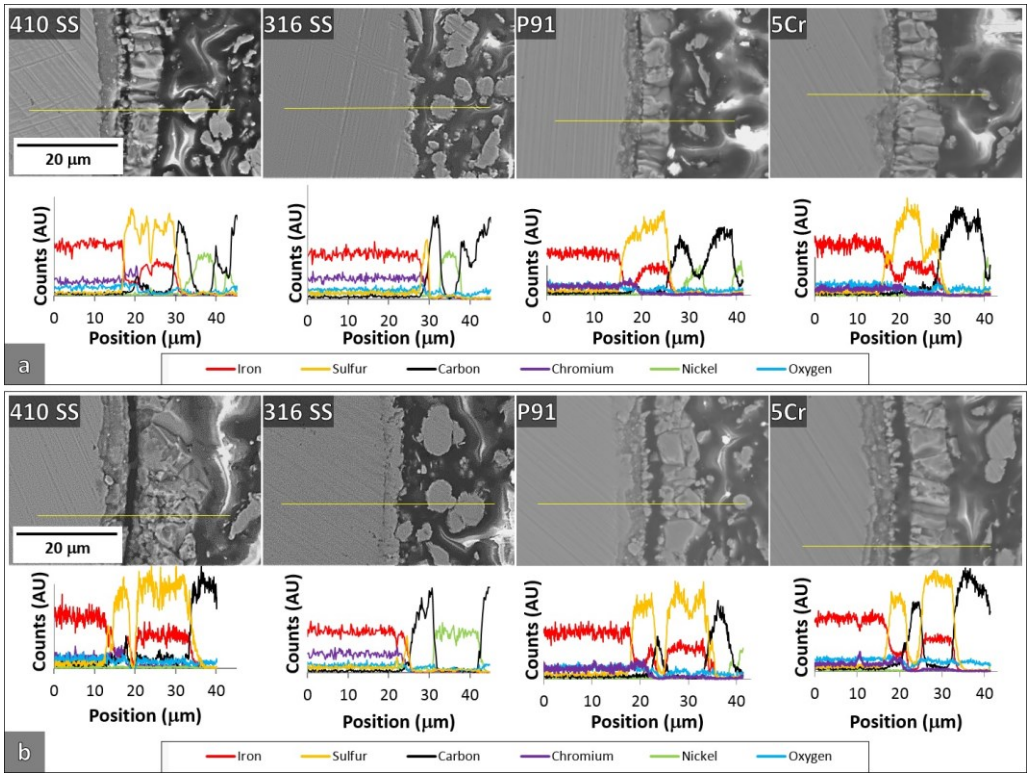

Figure 3.20: SEM micrographs of each metal reacted at medium-high temperature, for a long reaction time, with sulfur compounds (a) mercaptan 1, and (b) mercaptan 2.

Figure 3.20 shows the high magnification SEM micrographs and accompanying EDXS line scans for two mercaptans. These micrographs highlight the lack of reaction between these compounds and the 316 stainless steel, as discussed..

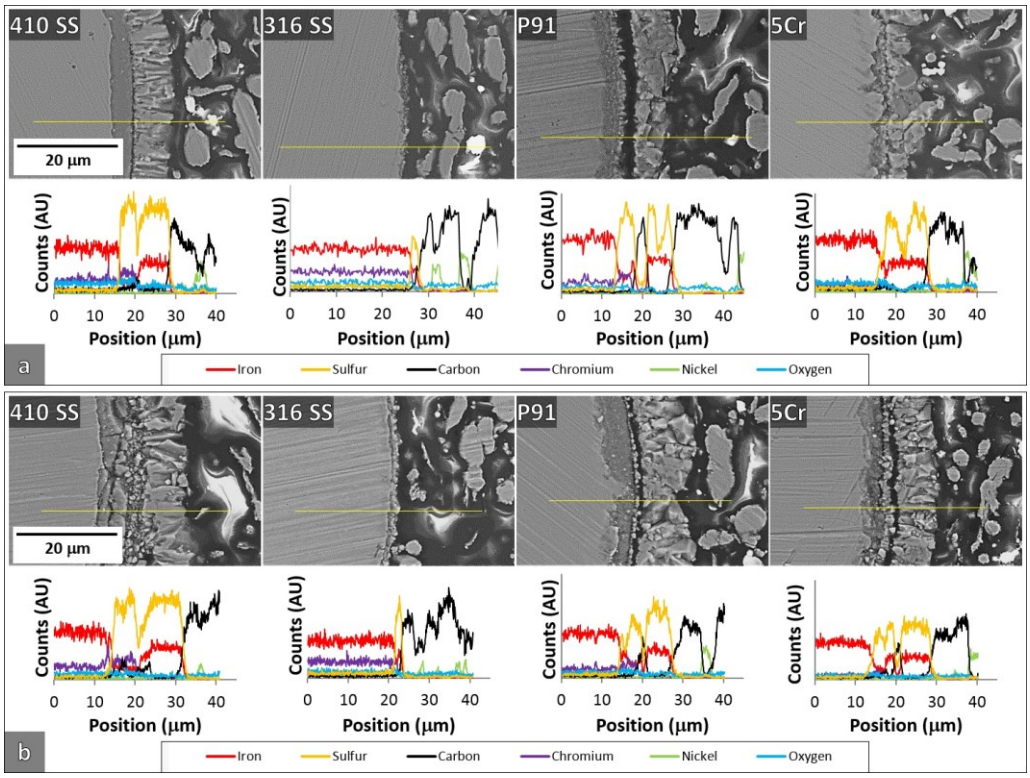

Figure 3.21: SEM micrographs of each metal reacted at medium-high temperature, for a long reaction time, with sulfur compounds (a) aliphatic sulfide, and (b) aliphatic disulfide.

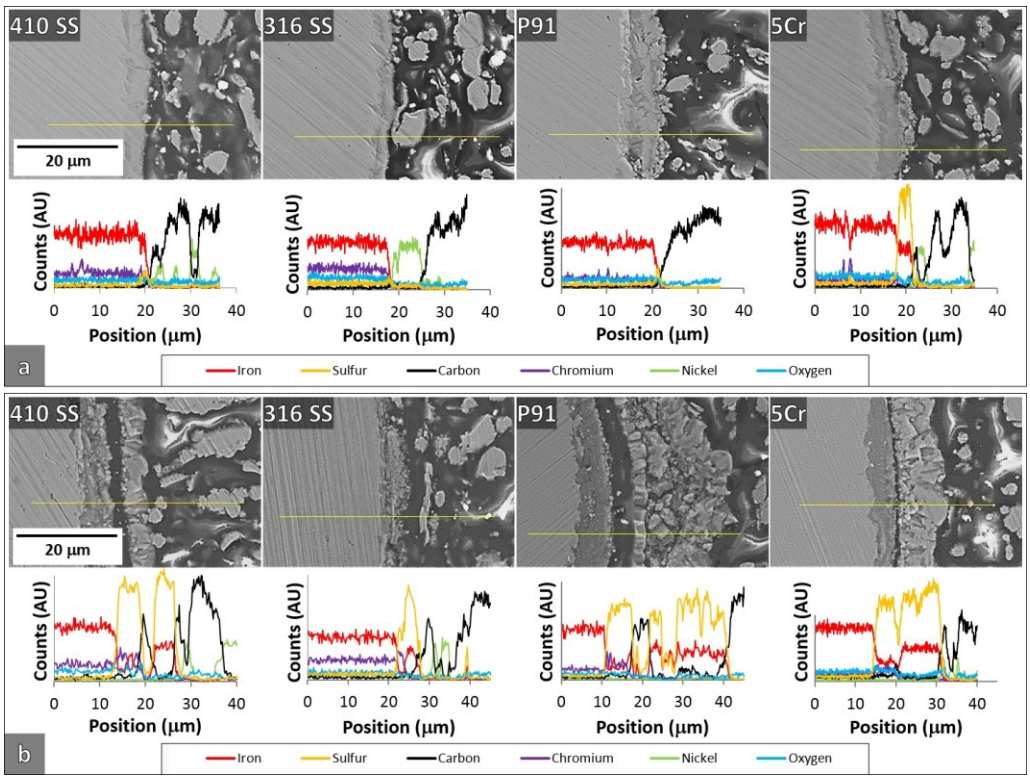

Figure 3.22: SEM micrographs of each metal reacted at medium-high temperature, for a long reaction time, with sulfur compounds (a) aromatic sulfide, and (b) aromatic disulfide.

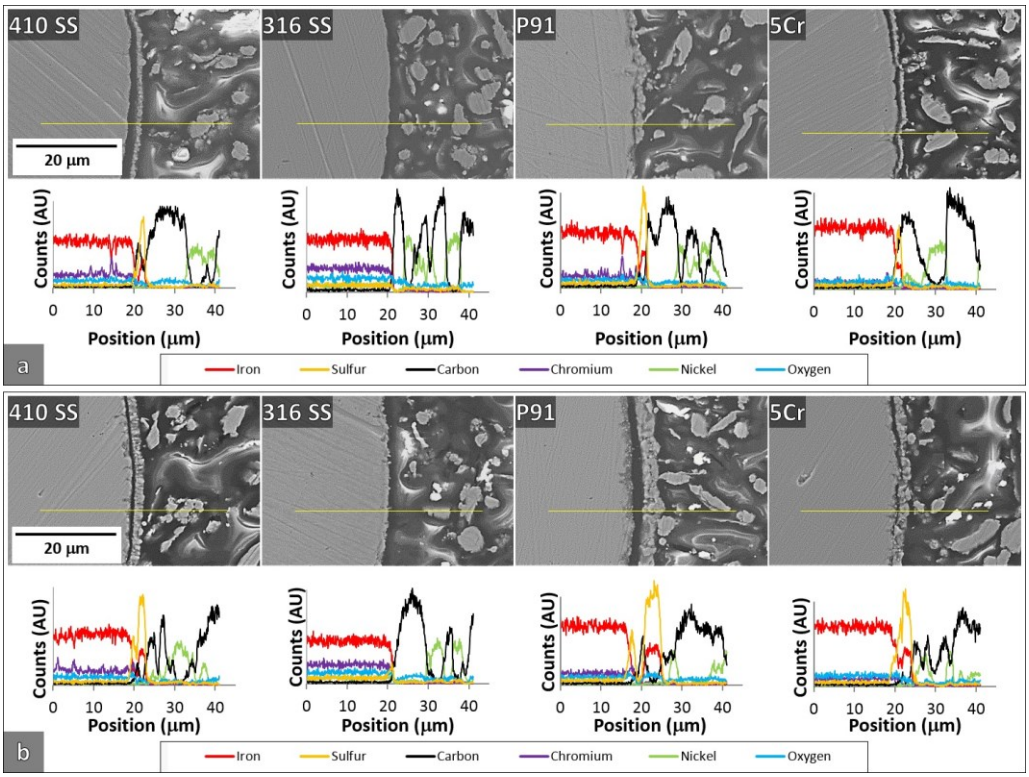

Figure 3.23: SEM micrographs of each metal reacted at medium-high temperature, for a long reaction time, with sulfur compounds (a) cyclic thioether 1, and (b) cyclic thioether 2.

While 410 stainless steel has enough chromium content to classify it as a stainless steel, it performed quite differently as compared to 316 stainless steel. It is generally known that martensitic steels are less corrosion resistant than austenitic steels, due to the absence of oxide-stabilizing Mo and Ni additives. Moreover 410 has much less Cr than 316, thus its oxide is expected to be less stable in an oxygen deficient reducing atmosphere such as hot mineral oil with H_2S gas or other reactive sulfur species. As seen in the micrographs, each sulfur compound, with the exception of aromatic sulfide, reacted with the 410. For instance aliphatic disulfide heavily corroded the surface, leaving slightly over 15 µm of iron sulfide, while the two cyclic thioethers produced only a thin layer. The carbon-steel, P91 and 5Cr steels showed a corrosion layer with every compound tested. This result is fairly expected, since they either don't display a protective surface oxide at all (carbon-steel, 5Cr, P91) or have one that is relatively unstable at test current test conditions (410), making the metallurgies susceptible to range of sulfidic attack mechanisms.

Figure 3.21 presents the high magnification micrographs and EDXS line scans for the aliphatic sulfide and aliphatic disulfide compounds. The aliphatic disulfide compound is the most corrosive species of the lot, producing a distinct sulfided corrosion layer even in the 316 SS. Micrographs and line scans for the aromatic sulfide and disulfide are presented in Figure 3.22. The results of the two cyclic thioethers are shown in Figure 3.23. Although neither of the compounds dissociated when tested without the metal wires and no H_2S was detected in the presence of the wires, some sulfidic attack is evident on all but the 316 wires. This substantiates the claim the while H_2S attack appears to be the most aggressive form of sulfidic corrosion encountered in this study, it is not the only path to producing iron sulfide on the metal surface.

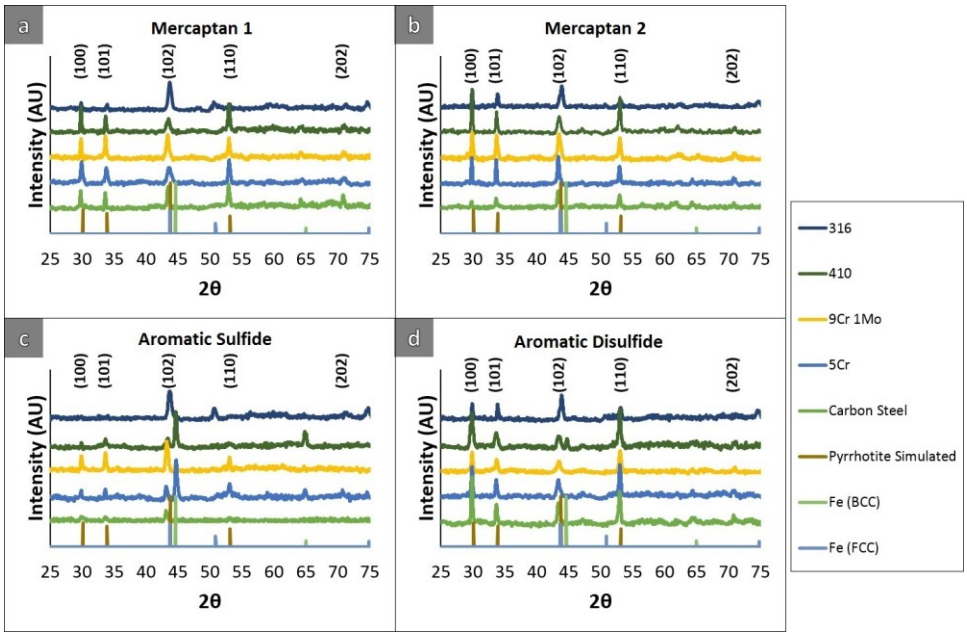

Figure 3.24: Master plot of all XRD scans of each metallurgy with each sulfur compound. (a),(b) Mercaptan 1 and 2. (c),(d) Aromatic sulfide and disulfide.

Figures 3.24 and 3.25 present the XRD scans for each combination of metal and sulfur compound, divided by sulfur compound. The pattern of each corroded metal contains iron sulfide peaks, with their relative intensity vs. the underlying metal matching the overall thickness of the sulfide layer. As for carbon-steel results, presented earlier, the peaks may be ascribed to either pyrrhotite or triolite, as they are isostructural and have similar lattice parameters. For the cases

where no corrosion was observed, the only peaks present correspond to the ferritic (carbon steel, 5Cr, P91), martensitic (410) and austenitic (316) wire metallurgies.

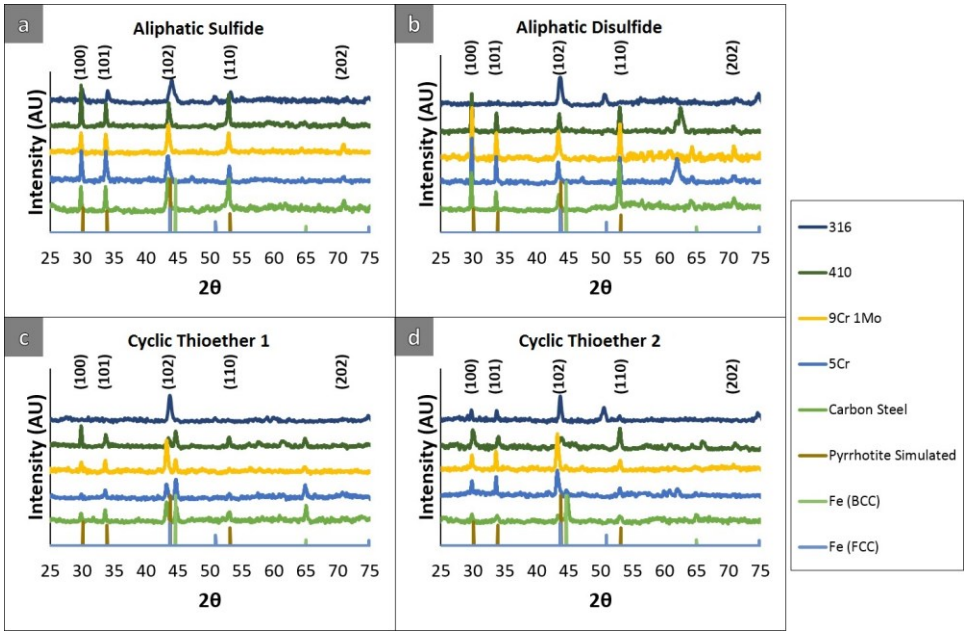

Figure 3.25: Master plot of all XRD scans of each metallurgy with each sulfur compound. (a),(b) Aliphatic sulfide and disulfide. (c),(d) Cyclic thioether 1 and 2.

3-5: H_2S Gas Corrosion

We further examined the details of H_2S corrosion by directly exposing each metallurgy to flowing H_2S. Each wire was placed in a sealed tube furnace with a flowing H_2S atmosphere (5174 ppmv H_2S, 10.19% hydrogen, argon balance) under various time and temperature conditions. The tube containing the wires was first purged with flowing Ar gas at a rate of 45 standard cubic centimeter per minute (sccm) for 30 minutes, followed by H_2S gas with the same parameters, followed by elevated temperature exposure at a flow rate of 5 sccm. Figures 3.26 – 3.29 show the cross-sectional micrographs of these results.

The 316 stainless steel, shown in Figure 3.27(a), is once again nearly pristine even after a long reaction at medium-high heat. The carbon-steel, shown in Figure 3.29(a), displayed a fairly stable sulfide layer with a neat thickness progression occurring at medium-high heat as the reaction time increased, with the longer experimental time correlating with a thicker sulfide layer.

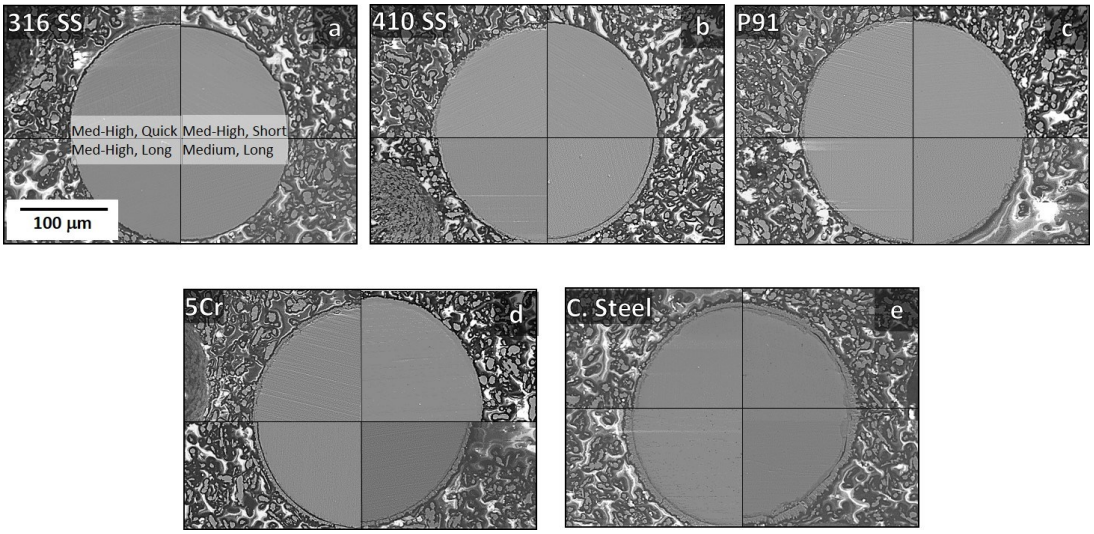

Figure 3.26: SEM micrograph cross-sections depicting the results of heating wires for various times and temperatures, with 5000 ppm H_2S gas flowing over the wires.

The other three metallurgies, 5Cr, P91 and 410, clearly showed some levels of surface sulfide formation, although with trends less obvious than for the carbon-steel. For instance, at the medium-high temperature, the thickness of the sulfide layer on 410 barely increased between the short and long reaction time. This may be in part due to a substantial portion of the sulfiding occurring at room temperature with the higher H_2S flow rate.

However, the overall trend in the relative corrosion resistance of the metallurgies is conclusive, as each material had an identical room temperature H_2S exposure. It was also observed that at medium heat and a long reaction time the carbon-steel, 5Cr, P91 and 410 specimens possessed a thicker sulfide layer than at medium-high heat and a long reaction time. This would be consistent with a spalling scenario, where at high temperatures the FeS is less adherent to the wire surface. The spallation hypothesis is consistent with the poor adhesion of the FeS layer observed on the four metals at medium-high heat. Alternatively, growth of FeS by the reaction of Fe and H_2S may intrinsically occur at higher rates at lower temperatures due to a higher sticking coefficient of the molecules. More work is needed to elucidate the true temperature dependence of H_2S attack.

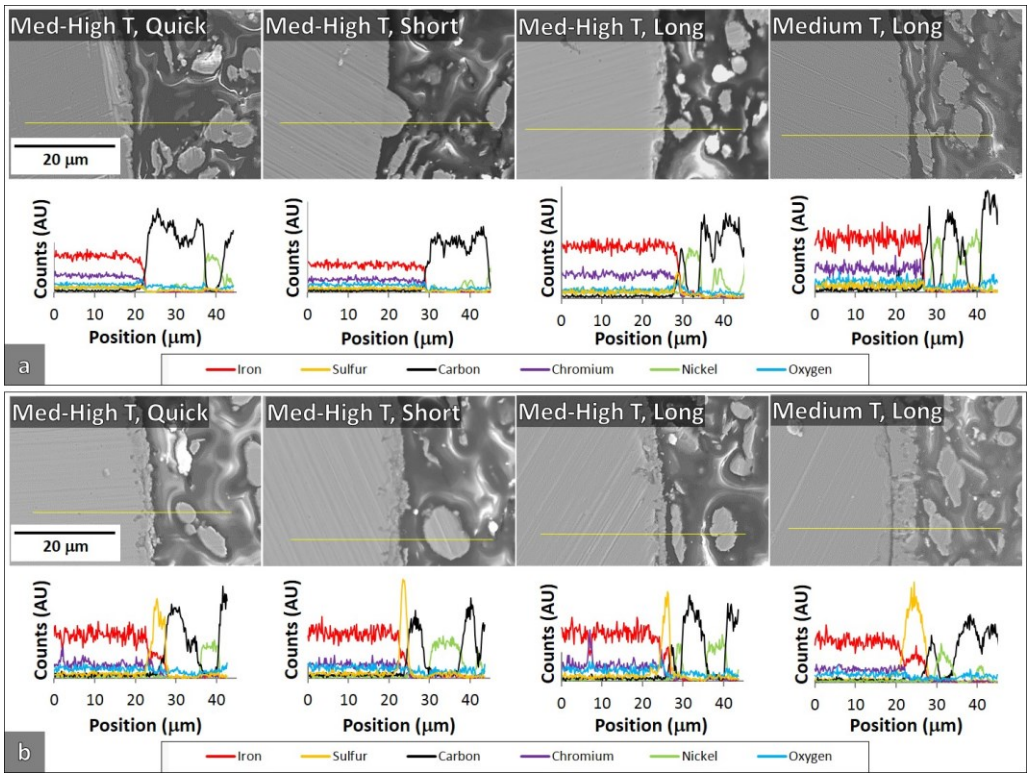

Figure 3.27: SEM micrographs and EDX line scans of wire cross-sections after H_2S exposure. (a) 316 stainless steel. (b) 410 stainless steel.

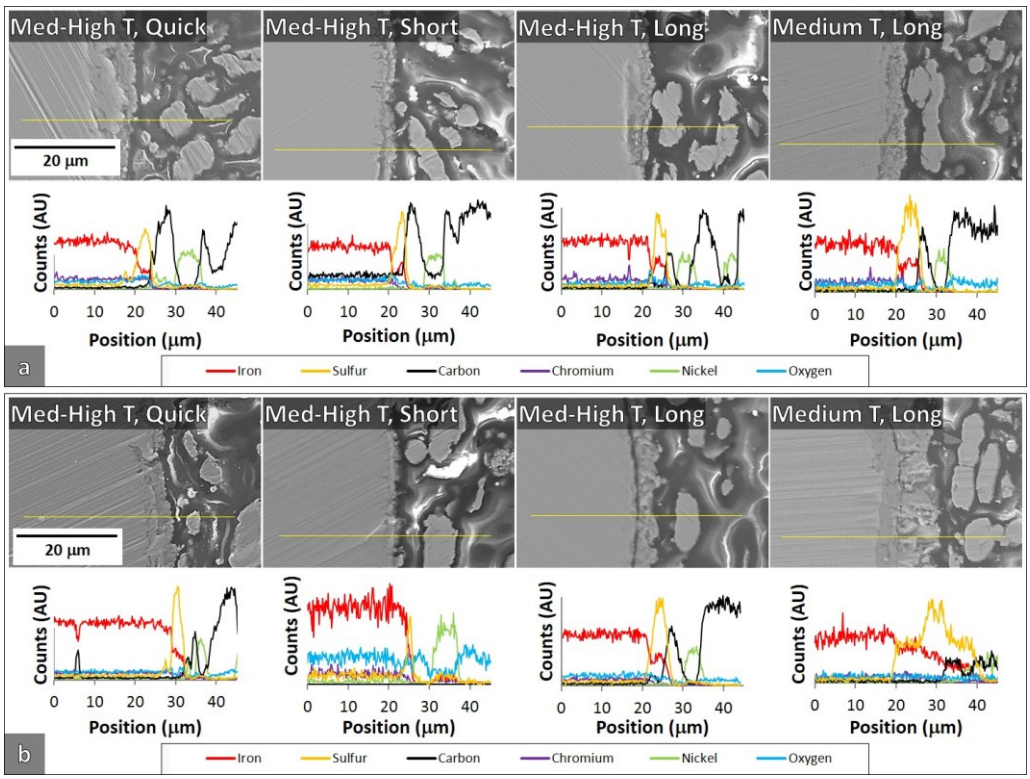

Figure 3.28: SEM micrographs and EDX line scans of wire cross-sections after H_2S exposure. (a) P91. (b) 5Cr.

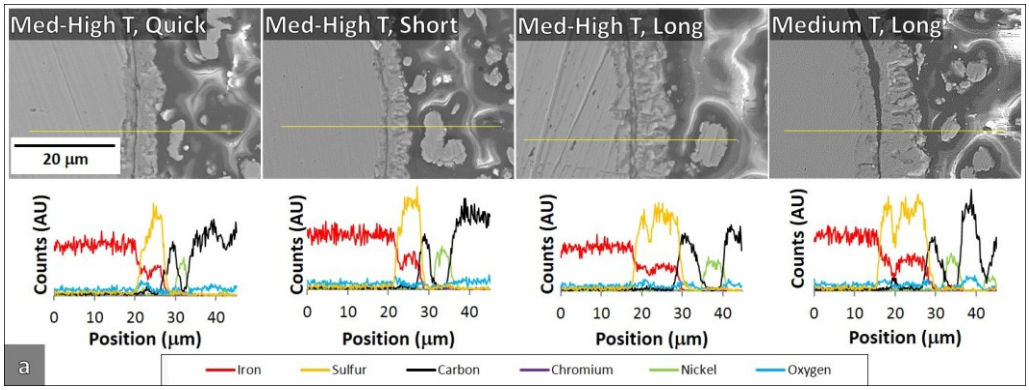

Figure 3.29: SEM micrographs and EDX line scans of wire cross-sections after H_2S exposure. (a) Carbon steel.

Chapter 4
Discussion

4-1: Non-H_2S Corrosion Mechanisms

The results of the corrosion experiments showed instances where sulfidic corrosion occurred on the surface of the metal in the absence of hydrogen sulfide. For instance, in the thermal decomposition experiments, we found that the two mercaptans did not produce hydrogen sulfide until slightly after the medium corrosion temperature. Yet clear corrosion layers formed on the carbon-steel samples under all experimental conditions tested. As indicated earlier, the presence of the metals in the reaction chamber may catalyze the decomposition to a lower temperature than what was measured from homogeneous decomposition experiments. However the intrinsic corrosivity of the sulfur compounds, without the need to form H_2S, should not be discounted.

There have been several earlier literature studies that posit a mechanism by which the compounds may attach Fe without an H_2S intermediate. For instance in ref.[54] authors examined the decomposition of methanethiol on a metal surface. A possible mechanism, illustrated in Figure 4.1, is that the thiol first loses its hydrogen. The two constituents, the hydrogen and the respective thiolate, then bond to the metal surface. This is supported by studies indicating that the S-H bond in methanethiol cleaves upon adsorption to a metal surface such as iron[54,55] or nickel.[56,57,58] From here, the C-S bond cleaves, leaving a sulfur atom strongly adsorbed to the surface, along with a free hydrogen and a surface hydrocarbon. Due to their close proximity, the strength of the bond between the sulfur atom and the surface metal likely weakens the bonding of the carbon-chain group and the surface metal, an effect noticed in particular with iron surfaces,[54,59] which readily bonds with the surface-bonded hydrogen. This can provide a possible explanation for the iron sulfide layers found on our carbon-steel samples without the presence of H_2S. An interesting result,

supported by authors in ref.[59] with their work on thiols, is that the difference in chain-length between the two mercaptans tested played no substantial role in resulting corrosion layer thickness, H_2S production, or decomposition temperature. On a pure Fe(100) surface, they noticed all straight-chain mercaptans longer than ethanethiol and onwards decomposed at the same temperature and produced hydrogen, hydrocarbons, and surface sulfur. This correlates well with our results, which showed that both mercaptans produced similar corrosion-layer thicknesses and broke down into hydrogen sulfide at the same temperature.

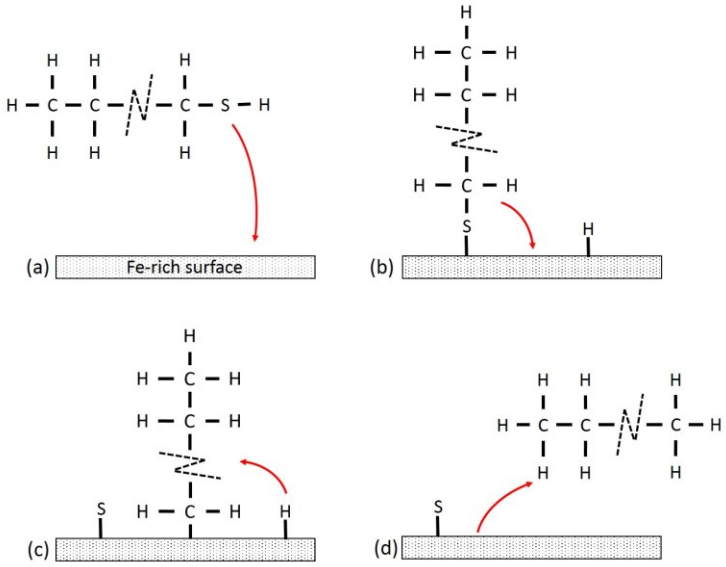

Figure 4.1: Graphic of decomposition mechanism for n-chain mercaptans.

A hypothesis related to this mechanism can possibly be extended to our results with the aliphatic disulfide and aromatic disulfide compounds. Given the stable nature of aromatics, there is possibly an absence of hydrogen in the system which limits hydrogen sulfide production in any decomposition or surface reactions. This is evidenced with the aromatic disulfide in particular, with hydrogen sulfide only being produced in small quantities during the long reaction time and medium-high temperature, A corrosion layer could maybe still form, for example, if the S-S bond in the disulfide cleaved, and the two aromatic-sulfur compounds each adsorbed onto the carbon-steel surface.

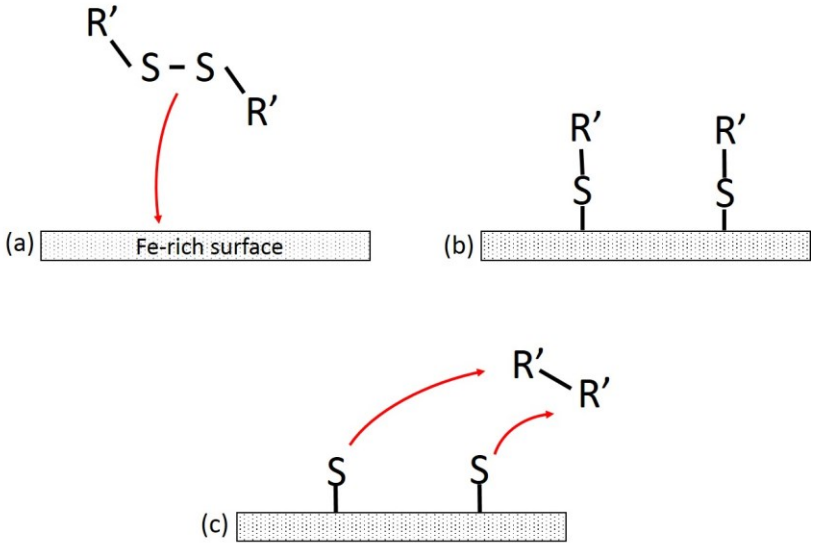

Figure 4.2: Graphic of possible decomposition mechanism for disulfides. (a),(b) Generic disulfide adsorbs onto the iron rich surface through cleavage of the sulfur-sulfur bond. (c) The sulfur-group bond cleaves preferentially to the sulfur-iron bond, releasing the remaining group in the oil and leaving sulfur on the iron surface.

This hypothetical adsorption reaction is illustrated in Figure 4.2. If the metal-sulfur bond was particularly strong, the aromatic group on each bonded sulfur might break off, and the two aromatic groups could possibly join to form a singular compound. This type of reaction could possibly hold for the aliphatic disulfide compound as well, with the major difference being that two aliphatic-group molecules would be released into the oil rather than the aromatic groups. A similar mechanism could be taking place with aromatic sulfide, with the exception that only one sulfur atom would be left on the surface at the end of the surface reaction. If this is true, this would fit with our experimental data. The aromatic disulfide compound corrosion layer thickness was systematically thicker than the aromatic sulfide corrosion layer thickness, which could possibly be a result of there being about twice as much sulfur on the surface to work with.

Chapter 5
Concluding Remarks

5-1: Concluding Remarks

In this thesis, the role of sulfur-based molecules and their corrosive nature has been studied, along with their interaction with various metallurgies relevant to the oil and gas industry.

The results of this work adds support to the well-known knowledge behind the thermal stability of cyclic thioethers. The two cyclic thioethers tested, C1 and C2, corroded each of the five metallurgies tested the least, and did not decompose into hydrogen sulfide gas at any tested temperature. The aliphatic disulfide compound, LD, on the other hand, resulted in being the most corrosive sulfur compound and the compound that most readily decomposed into hydrogen sulfide. This is likely due to the combination of the lack of stable aromatic groups, the overall disulfide structure, and the particular structure of the aliphatic functional groups.

Of the different metallurgies tested, the 316 stainless steel was the most corrosion-resistant, as was expected. The carbon steel was the least corrosion-resistant, with corrosion only slightly decreasing in the 5Cr and 9Cr alloys, with their increased chromium content. Although the 410 steel has a relatively large amount of chromium and can technically be classified as a stainless steel, this steel corroded quite heavily in our experiments. This is likely due to the martensitic structure of the 410 steel.

Future work on this topic could look at quantifying the decomposition of the sulfur compounds into hydrogen sulfide more precisely, perhaps through the use of a thermogravimetric analysis system with a constant heating rate and hydrogen sulfide detection system.

References

[1] Eden D. Pipelines corrosion - Real-time monitoring of corrosion in the pipeline. Pet Rev 2001;55:27–9.

[2] McCafferty E. Introduction to Corrosion Science. Alexandria, VA, USA: Springer Science+Business Media; 2010. doi:10.1007/978-1-4419-0455-3.

[3] Popoola L, Grema A, Latinwo G, Gutti B, Balogun A. Corrosion problems during oil and gas production and its mitigation. Int J Ind Chem 2013;4:35. doi:10.1186/2228-5547-4-35.

[4] Simmons MR. Oil And Gas "Rust": An Evil Worse Than Depletion. Offshore Technol. Conf., Houston, Texas: 2008.

[5] Deshannavar UB, Rafeen MS, Ramasamy M, Subbaro D. Crude Oil Fouling: A Review. J Appl Sci 2010;10:3167–74.

[6] Tay FH, Kazarian SG. Study of Petroleum Heat-exchanger Deposits with ATR-FTIR Spectroscopic Imaging. Energy & Fuels 2009;23:4059–67. doi:10.1021/ef900304v.

[7] Awad MM. Fouling of Heat Transfer Surfaces. In: Belmiloudi A, editor. Heat Transfer - Theoretical Analysis, Experimental Investigations and Industial Systems, InTech; 2011, p. 505–42. doi:10.5772/13696.

[8] Yang J, Serratos MGJ, Fari-Arole DS, Müller EA., Matar OK. Crude Oil Fouling: Fluid Dynamics, Reactions and Phase Change. Procedia IUTAM 2015;15:186–93. doi:10.1016/j.piutam.2015.04.026.

[9] Gentzis T, Parker RJ, McFarlane RA. Microscopy of fouling deposits in bitumen furnaces. Fuel 2000;79:1173–84. doi:10.1016/S0016-2361(99)00225-2.

[10] E H, Watkinson AP. Precipitation and Fouling in Heavy Oil–Diluent Blends. Heat Transf Eng 2009;30:786–93. doi:10.1080/01457630902744143.

[11] Wang Y, Yuan Z, Liang Y, Xie Y, Chen X, Li X. A review of experimental measurement and prediction models of crude oil fouling rate in crude refinery preheat trains. Asia-Pacific J Chem Eng 2015;10:607–25. doi:10.1002/apj.1895.

[12] Kazi SN. Fouling and Fouling Mitigation on Heat Exchanger Surfaces. In: Mitrovic J, editor. Heat Exch. - Basics Des. Appl., InTech; 2012, p. 507–32. doi:10.5772/32990.

[13] Khan MS, Zubair SM, Budair MO, Sheikh AK, Quddus A. Fouling resistance model for prediction of CaCO3 scaling in AISI 316 tubes. Heat Mass Transf 1996;32:73–9. doi:10.1007/s002310050094.

[14] Sheikholeslami R. Composite fouling - inorganic and biological: A review. Environ Prog 1999;18:113–22.

[15] Coetser SE, Cloete TE. Biofouling and Biocorrosion in Industrial Water Systems. Crit Rev Microbiol 2005;31:213–32. doi:10.1080/10408410500304074.

[16] Rahmani S, McCaffrey WC, Dettman HD, Gray MR. Coking kinetics of asphaltenes as a function of chemical structure. Energy and Fuels 2003;17:1048–56. doi:10.1021/ef030007c.

[17] Speight JG. The Desulfurization of Heavy Oils and Residua. Second Edi. Laramie, Wyoming, USA: Marcel Dekker Inc.; 2000.

[18] Gray MR. Upgrading Oilsands Bitumen and Heavy Oil. First Edit. Edmonton, Alberta, Canada: University of Alberta Press; 2015.

[19] Wiehe IA. Process Chemistry of Petroleum Macromolecules. Boca Raton, Florida, USA: CRC Press; 2008.

[20] Speight JG. High Acid Crudes. Laramie, Wyoming, USA: Gulf Professional Publishing; 2014. doi:10.1016/B978-0-12-800630-6.00004-6.

[21] Gray MR, Khorasheh F, Wanke SE. Role of catalyst in hydrocracking of residues from Alberta bitumens. Energy & Fuels 1992;6:478–85. doi:10.1021/ef00034a019.

[22] Foroulis ZA. High temperature degradation of structural materials in environments encountered in the petroleum and petrochemical industries: Some mechanistic observations. Anti-Corrosion Methods Mater 1985;32:4–9. doi:10.1108/eb020393.

[23] Gutzeit J, Merrick R, Scharfstein L. Corrosion in Petroleum Refining and Petrochemical Operations. Corrosion Vol.13, Metals Handbook, ASM International; 1987, p. 1262.

[24] Lewis KR, Daane ML, Schelling R. Processing Corrosive Crude Oils. NACE Corros Conf 1999;377:1–10.

[25] Zetlmeisl MJ, Harrell JB, Campbell J. Naphthenic Acid Corrosion Control. Hydrocarb Eng 2000:41–5.

[26] Li H, Chen W. Effect of Sulfur Partial Pressures on Oxidation Behavior of Fe–Ni–Cr Alloys. Oxid Met 2012;78:103–22. doi:10.1007/s11085-012-9294-6.

[27] Gesmundo F, Bregani F, Viani F, Znamirowski W, Godlewski K. The Corrosion of Iron and of Three Commercial Steels in H2-H2S and H2-H2S-CO2 Gas Mixtures at 400-700 C. Mater Corros 1992;43:83–95.

[28] Orchard J, Young D. Gas-Phase Composition Effects on the Iron Sulfide Scaling Reaction. J Electrochem Soc 1986;133:1734. doi:10.1149/1.2109005.

[29] Lobnig RE, Grabke HJ. Mechanisms of simultaneous sulfidation and oxidation of Fe-Cr and Fe-Cr-Ni-alloys and of the failure of protective chromia scales. Corros Sci 1990;30:1045–71. doi:10.1016/0010-938X(90)90211-M.

[30] Baxter DJ, Natesan K. Breakdown of chromium oxide scales in sulfur-containing environments at elevated temperatures. Oxid Met 1989;31:305–23. doi:10.1007/BF00846691.

[31] Wilson DF, Devereux OF. High-Temperature Sulfidation of Iron in H2/H2S/CO/C02 Mixtures. J Electrochem Soc 1991;138:2168–76.

[32] Farrell D, Roberts L. A Study Of High Temperature Sulfidation Under Actual Process Conditions. NACE Corros Conf 2010;10358:1–11.

[33] Gutzeit J. High temperature sulfidic corrosion of steels. NACE, Process Ind Corros Theory Pract 1986:367–72.

[34] Lai GY. High-Temperature Corrosion and Materials Applications. High-Temperature Corros. Mater. Appl. First Edit, Ohio 44073-0002: ASM International; 2007, p. 201–31.

[35] Stephenson TJ, Kubis A, Derakhshesh M, Hazelton M, Holt C, Eaton P, et al. Corrosion-Fouling of 316 Stainless Steel and Pure Iron by Hot Oil. Energy & Fuels 2011:4540–51.

[36] Kapusta SD, Ooms A, Smith A, Fort WC. Safe Processing of High Acid Crudes. NACE Corros Conf 2004;04637:1–19.

[37] de Jong J, Dowling N, Sargent M, Etheridge A, Saunders-Tack A, Fort W. Effect of Mercaptans and other organic sulfur species on high temperature corrosion in crude and condensate distillation units. NACE Corros Conf 2007;07565:1–7.

[38] Dettman HD, Li N, Luo J. Refinery Corrosion, Organic Acid Structure, and Athabasca Bitumen. NACE Corros Conf 2009;09336:1–13.

[39] Dettman HD, Luo J. The Influence of Napthenic Acid and Sulfur Compound Structure on Global Crude Corrosivity under Vacuum Distillation Conditions. NACE Corros Conf 2012;C2012-0001:1–15.

[40] García-Antón J, Monzó J, Guiñón JL. Effect of Elemental Sulfur and Mercaptans on Copper Strip Corrosion and Use of the ASTM D 130 Test Method. Corrosion 1995;51:558. doi:10.5006/1.3294376.

[41] Abe F. 18Cr-12Ni-Mo steel. In: Yagi K, Merckling G, Kern T-U., Irie H, Warlimont H, editors. Creep Prop. Heat Resist. Steels Superalloys, Springer; 2004, p. 227–46. doi:10.1007/b80641.

[42] Abe F. High Cr steels. In: Yagi K, Merckling G, Kern T-U., Irie H, Warlimont H, editors. Creep Prop. Heat Resist. Steels Superalloys, Springer; 2004, p. 144–9. doi:10.1007/b80641.

[43] Yagi K. 5Cr-0.5Mo steel. In: Yagi K, Merckling G, Kern T-U., Irie H, Warlimont H, editors. Creep Prop. Heat Resist. Steels Superalloys, Springer; 2004, p. 87–9. doi:10.1007/b80641.

[44] Memon HUR, Williams A, Williams PT. Shock tube pyrolysis of thiophene. Int J Energy Res 2003;27:225–39. doi:10.1002/er.870.

[45] Winkler JK, Karow W, Rademacher P. Gas-phase pyrolysis of heterocyclic compounds, part 1 and 2: Flow pyrolysis and annulation reactions of some sulfur heterocycles: Thiophene, benzo[b]thiophene, and dibenzothiophene. A product-oriented study. J Anal Appl Pyrolysis 2002;62:123–41. doi:10.1016/S0165-2370(00)00218-7.

[46] Barckholtz C, Barckholtz TA., Hadad CM. C-H and N-H bond dissociation energies of small aromatic hydrocarbons. J Am Chem Soc 1999;121:491–500. doi:10.1021/ja982454q.

[47] Xia D, Tian Y, Zhu G, Xiang Y, Luo L, Huang TT-S. Theoretical and experimental studies on the thermal cracking of tetrahydrothiophene. Energy & Fuels 2007;21:1–6. doi:10.1021/ef060095b.

[48] Yang B, Tian S, Zhao S. A study of thermal decomposition of alkanethiols in pressure reactor. Fuel Process Technol 2006;87:673–8. doi:10.1016/j.fuproc.2004.11.018.

[49] Hudzik JM, Bozzelli JW, Simmie JM. Thermochemistry of C7H16 to C10H22 alkane isomers: Primary, secondary, and tertiary C-H bond dissociation energies and effects of branching. J Phys Chem A 2014:9364–79.

[50] Chandrasiri JA, Wilkie CA. Thermal degradation of diphenyl disulfide and a blend of diphenyl disulfide with poly)methyl methacrylate). Polym Degrad Stab 1994;46:275–84.

[51] Plaza S, Celichowski G, Margielewski L, Leśniak S. Flash thermolysis of dibenzyl and diphenyl disulphides. Wear 2000;237:295–9. doi:10.1016/S0043-1648(99)00358-0.

[52] Plaza S, Gruziński R. Homogeneous and heterogeneous thermal decomposition of diphenyl disulphide. Wear 1996;194:212–8. doi:10.1016/0043-1648(95)06859-7.

[53] Furka Á. Relative energy of organic compounds II. Halides, nitrogen, and sulfur compounds. Struct Chem 2009;20:605–16. doi:10.1007/s11224-009-9450-z.

[54] Albert MR, Lu JP, Bernasek SL, Cameron SD, Gland JL. The mechanism of the decomposition of methanethiol on Fe(100). Surf Sci 1988;206:348–64. doi:10.1016/0039-6028(88)90138-0.

[55] Meagher KK, Bocarsly AB, Bernasek SL, Ramanarayanan TA. Interaction of Neopentyl Thiol with Clean and Oxygen-Modified Fe(100) Surfaces †. J Phys Chem B 2000;104:3320–6. doi:10.1021/jp993335f.

[56] Castro ME, White JM. Decomposition of methanethiol on Ni(111): a TPD and SSIMS study. Surf Sci Lett 1991;257:A561. doi:10.1016/0167-2584(91)91086-C.

[57] Lock JA, Woodruff JR. Adsorption and Reactions of Methanethiol on Clean and Modified Ni(110). Appl Opt 1989;28:523–9.

[58] Castro ME, White JM, Ahkter S, Golchet A, Sahin T. Methanethiol Decomposition on Ni(100). Langmuir 1991:126–33.

[59] Cheng L, Bocarsly AB, Bernasek SL, Ramanarayanan TA. Interaction of Alkanethiols with Single Crystal Iron: The Low-Temperature Decomposition of Ethanethiol on the Fe(100) Surface. Langmuir 1994:4542–50.